SMAP Radiometer Brightness Temperature Calibration for the L1B_TB (Version 5), L1C_TB (Version 5), and L1C_TB_E (Version 3) Data Products
Soil Moisture Active Passive (SMAP) Project

Citation:

Jinzheng Peng, Sidharth Misra, Steven Chan, Julian Chaubell, Rajat Bindlish, Alexandra Bringer, Andreas Colliander, Giovanni De Amici, E.P. Dinnat, Derek Hudson, Tom Jackson, Joel Johnson, David Le Vine, Thomas Meissner, Priscilla Mohammed, Jeffrey Piepmeier, Dara Entekhabi, Simon Yueh, August 8, 2020. *SMAP Radiometer Brightness Temperature Calibration for the L1B_TB, L1C_TB (Version 5), and L1C_TB_E (Version 3) Data Products*, SMAP Project, Jet Propulsion Laboratory, Pasadena, CA. [Online.] https://nsidc.org/data/smap/data_versions.

August 8, 2020

JPL-D 56295

Contributors to this report:

Rajat Bindlish[1], Alexandra Bringer[5], Steven Chan[2], Julian Chaubell[2], Andreas Colliander[2], Giovanni De Amici[1], E.P. Dinnat[1,6], Dara Entekhabi[9], Derek Hudson[1], Tom Jackson[4], Joel Johnson[5], David Le Vine[1], Thomas Meissner[7], Sidharth Misra[2], Priscilla Mohammed[1,8], Jinzheng Peng[1,3], Jeffrey Piepmeier[1], Simon Yueh[2]

[1]NASA's Goddard Space Flight Center, Greenbelt, MD 20771 USA
[2]Jet Propulsion Laboratory, California Institute of Technology, Pasadena, CA 91109 USA
[3]Universities Space Research Association, Columbia, MD 21046 USA
[4]USDA ARS Hydrology and Remote Sensing Lab, Beltsville, MD 20705 USA
[5]The Ohio State University, Electrical and Computer Engr., Columbus, OH 43210 USA
[6]Center of Excellence in Earth Systems Modeling and Observations, Chapman University, Orange, CA 92866 USA
[7]Remote Sensing Systems, Santa Rosa, CA 95401 USA
[8]Morgan State University, Baltimore, MD 21251 USA
[9]Massachusetts Institute of Technology, Department of Civil and Environmental Engineering, Cambridge, MA, 02139 USA

Executive Summary

This report provides analysis and assessment of calibration quality of SMAP radiometer brightness temperatures available in the L1B_TB and L1C_TB version 5 data products for over four years of data. The key innovation is an improvement in calibration components. The calibration changes can be summarized as follows: (1) Used radiometer's internal reference load as the hot calibration source instead of the global ocean used in Version 4, and (2) Concurrent calibration of all calibration parameters (antenna pattern correction (APC), noise-diode and SMAP reflector emissivity). Calibration methods also include different types of cold sky calibration.

Calibration stability is assessed using ocean targets. Geolocation is verified using conventional coastal-crossing analysis. Performance of radio-frequency interference (RFI) mitigation is done using statistical analysis. Overall validation is performed using comparisons to the Soil Moisture and Ocean Salinity (SMOS) and Aquarius radiometer data.

Geolocation performance meets requirements with ample margin. Ocean and cold-sky drift analysis reveals time-varying gain and offset drifts of less than 0.1K. RFI mitigation is performing well. The calibration meets with margin the mission requirement error budget of <1.8 K rms (per footprint). The report finds that the radiometer calibration compares favorably with SMOS over land, ocean, and ice with differences < 0.6 K overall and ~1.64 K on average (2.37 K for V-pol and 0.90 K for H-pol) over land. The 9-km gridded L1C_TB_E product is based on the L1B_TB product and unchanged from previous release.

1 Introduction

This document provides a calibration assessment of the Version 5 product and an assessment of the enhanced brightness temperature product L1C_TB_E.

The primary validation assessment is performed comparing the calibrated data to the ocean brightness temperature model. Favorable comparison to SMOS over land and ocean provide additional validation. The instrument continues to perform as expected. Both geolocation accuracy and NEDT meet the project requirements. Comparison with SMOS reveals a 2.37 K (V-pol) and 0.90 K cold difference (over land), which is a brightness temperature (TB) decrement from Version 4. SMAP brightness temperatures continue to enable reasonable soil moisture retrieval performance. A concise summary of the current performance is listed in Tables 1.1 & 1.2. Comparing to the previous versions, the global averaged TB changes over the Earth's surface are listed in Table 1.3.

Table 1.1: Performance of SMAP Radiometer Level 1B Brightness Temperature Data.

Parameter	Version 5	Requirement
NEDT (over land)	1.1 K	< 1.6 K
Geolocation accuracy	2.7 km	< 4 km
Ocean Model STD*	1.1 K	< 1.4 K
Land SMAP/SMOS comparison (H pol)	-0.90 K	n/a
Land SMAP/SMOS comparison (V pol)	-2.37 K	n/a

Table 1.2: Assessment of SMAP Radiometer Level 1C Enhanced Brightness Temperature Data.

Parameter	Version 3
NEDT (over ocean)	0.7 K
Bias with respect to L1B_TB	+/- 3 mK

Table 1.3.   TB change in Version 5 comparing to the previous versions

	Land		Ocean	
	V-Pol	H-Pol	V-Pol	H-Pol
Version 3	0.0 K	1.0 K	-1.4 K	-1.4 K
Version 4	-2.8 K	-2.3 K	-1.4 K	-0.6 K

Note: Negative sign means that TB of Version 5 is lower.

2   Geolocation Assessment

The geolocation requirement for a radiometer footprint is to have knowledge of uncertainty of less than 4 km (interpreted as the not-to-exceed value). The geolocation error is defined as the absolute Cartesian distance between the location reported in the L1B product and an image-processing-derived location in planar geometry. This section provides an assessment of the geolocation performance of the SMAP radiometer system.

The requirement was verified via a comparison of the reported geolocation of the instrument's footprints against the radiometric antenna (or brightness) temperature data at and near coastlines. The assumption underlying this approach is that the antenna temperature will undergo a quick change (from high-to-low) as the instrument's footprint passes from land to water. When the coastline is straight (at the spatial resolution of the footprint) and free of near-shore islands or lakes or rivers, the shape of the change corresponds to the convolution of the antenna's beam gain pattern with a step function, which is mathematically represented as a sigmoid curve. For a reasonably symmetric antenna beam, the midpoint of the sigmoid represents both the largest gradient in temperature and the location of the land/water boundary. This technique has been used successfully to verify the geolocation of heritage satellite-borne microwave instruments [2.1 – 2.6]. The novelty here is represented by SMAP full-circle scan, which ensures that whenever a positive (water-to-land) temperature gradients is present within a scan, a corresponding negative (land-to-water) gradient follows (or precedes) within the same or subsequent scan, a few seconds to two and half minutes later.

The algorithm was first "trained" on simulated data, designed to represent a realistic image of the operational measurements. The training showed that the latitude/longitude ranges allowed for a valid detection and the steepness of the sigmoid curve required before a crossing is considered do affect the quality and quantity of the detections. The former is needed to exclude areas where islands, rivers, lakes produce false identifications, the latter to eliminate orbits that are only tangent to the coastline. The results shown here are robust to small changes in the detection parameters.

Figure 2.1: Examples of selected ascending/descending half orbits whose ground tracks are either near-perpendicular or near-parallel to geographical coastlines. The resulting transition of the sigmoid curve was used to evaluate the geolocation accuracy of the SMAP radiometer.

For this analysis a set of 13 half-orbits was selected to represent overpasses of both N-S and E-W aligned coastlines, along ascending and descending paths. The areas chosen are the Southwest and West coasts of Africa, the East coast of Madagascar, and the West and South coasts of Australia; they are shown in Fig. 2.1 together with the identifiers for the half-orbit files. The common characteristic among these 13 orbits is a near-perpendicular or near-parallel direction of the satellite ground track with respect to the coastline. This ensures that either the edge or the central part of the swath crosses perpendicular to the geographical coastline.

The capability of the algorithm was validated against a corresponding set of control orbits from the reported geolocation information. In these orbits, the radiometric data field is replaced by a number which represents the integration of a digital water fraction map (resolution 0.01 deg) with a 2-D Gaussian with major and minor axes that match the projected SMAP antenna footprint; an ocean footprint has value of unity.

Table 2.1: Determination of geolocation error based on simulated water-fraction data.

Coastline direction	Geographical Area	Orbit #	Coast Geolocation Error (km)	Number of Detected Crossings
N-S	SW Africa	1369_D	2.27	200
	W Australia	1394_D	1.82	78
	Madagascar	1405_A	2.61	150
	SW Africa	1413_D	2.18	192
	W Australia	1417_A	2.13	68
	Madagascar	1426_D	2.08	116
	Madagascar	1470_D	2.61	109
E-W	W Africa	1363_A	2.39	78
	Australia	1364_D	2.01	77
	W Africa	1370_D	2.59	165
	Australia	1402_A	2.96	68
	W Africa	1407_A	2.75	96
	Australia	1452_D	2.16	71
Average			2.35	

For each coastline/orbit combination, the algorithm reports the number of detected crossings and the average absolute distance between each crossing and the nearest true coastline edge, as determined from the finest resolution Global Self-consistent Hierarchical High-resolution Shoreline (GSHHS) map. Table 2.1 shows the results from running the algorithm over the simulated water-fraction data. Each orbit yields at least 68 detections and the uncertainty in the position of the coastline is always smaller than 3 km. The average uncertainty of all detections is 2.35 km – a remarkably small error for footprints that are 35 km wide (HPBW) and sampled every 13 km. Since the water-fraction map and the Gaussian beam pattern are known *a priori* with the highest precision, the error of 2.35 km (less than 7% of footprint size) can be considered the theoretical best achievable by the algorithm on the SMAP footprint. The technique and algorithm discussed here present very good sensitivity to yaw (or clocking) errors, good

sensitivity to pitch and roll errors, and almost no sensitivity to errors in the opening angle of the scan cone.

Table 2.2 shows the results of applying the algorithm to a set of operational data, with the geolocation as reported in the L1B files and after applying a small (0.13 deg) counterclockwise yaw correction to the geolocation data. The average uncertainty for the first set of results is 2.73 km, and for the second is 2.45 km. The beta data do not contain the yaw correction and perform as indicated in the first column (i.e., 2.73 km). The actual data, which are inclusive of instrument noise, only increase the geolocation uncertainty to 7% of the footprint.

Table 2.2: Determination of geolocation error after small yaw correction.

Coastline direction	Geographical Area	Orbit #	Coast Geolocation Error (km)	After Yaw Adjustment (km)
N-S	SW Africa	1369_D	2.55	2.77
	W Australia	1394_D	1.55	1.80
	Madagascar	1405_A	3.06	2.10
	SW Africa	1413_D	2.33	2.62
	W Australia	1417_A	2.03	1.75
	Madagascar	1426_D	2.18	1.57
	Madagascar	1470_D	3.48	3.10
E-W	W Africa	1363_A	3.05	2.96
	Australia	1364_D	3.09	2.13
	W Africa	1370_D	3.13	2.85
	Australia	1402_A	3.54	3.28
	W Africa	1407_A	2.75	2.37
	Australia	1452_D	2.67	2.49
Average			2.73	2.45

References

[2.1] Moradi, I., et al., "Correcting Geolocation Errors for Microwave Instruments aboard NOAA Satellites", *IEEE TGRS*, 51, 3625, June 2013.

[2.2] Poe, G.A., and R. W. Conway, "A study of the geolocation errors of the special sensor microwave/imager (SSM/I)," *IEEE TGRS*, 28, 5, 791–799, September 1990.

[2.3] Poe, G.A. et al., "Conical Microwave Imaging/Sounding: Geo-location Error Analysis", 2003 (NPOESS Internal Government Study, unpublished)

[2.4] Poe, G.A., et al., "Geolocation error analysis of the special sensor microwave imager/sounder," *IEEE TGRS*, 46, 913–922, April 2008.

[2.5] Purdy, W. E., et al., "Geolocation and pointing accuracy analysis for the WindSat sensor," *IEEE TGRS*, 44, 496–505, March 2006.

[2.6] Wiebe, H., G. Heygster and L. Meyer-Lerbs, "Geolocation of AMSR-E data," *IEEE TGRS,* 46, 3098–3103, October 2008.

3   Drift Removal in T_{ND}

Comparing to the calibration for Version 3 which uses the global ocean to calibrate the internal noise source after adjusted the antenna gain (or front-to-back ratio) using a special cold sky calibration [3.1], and the calibration for Version 4 which concurrently calibrate Tnd, the antenna gain (or front-to-back ratio) and additional offset temperature, Trefl_offset, of the internal reference loads at the same time after the reflector emissivity (or loss factor) had been calibrated [3.2], the calibration for Version 5 has been upgraded to use the observations from multiple scenes (normal CSC, and special CSC) to solve for the internal noise source brightness temperature Tnd, the antenna gain (or front-to-back ratio) and the reflector emissivity (or loss factor) concurrently. Constant calibration values are used after July 7, 2015; there is a one time update of Trefl_offset to compensate unwanted signal from SAR transmitter when it's on, and there is a daily update to Tnd prior July 7, 2015 to remove the drift and bias in Tnd.

It was observed that the measured T_A's were drifting comparing to the ocean L-band GMF model [3.3]. The drifts are about 0.31 K/month for V-pol and 0.39 K/month for the first two months, and the radiometer is stabilized thereafter. The drift and bias from April 1 to June 15, 2015 are shown in Figure 3.1a. The drift is removed by the daily updated T_{ND}. The residual calibration drift over global ocean is shown in Figure 3.1b, and its uncertainty is 0.05 K for V-pol and 0.07 K for H-pol. The biases in δT_A over the global ocean are adjusted to -1.22 K for V-pol and -1.05 K for H-pol which are matched with the biases in the calibration drift over the global ocean after July 7, 2015, and they are most likely due to the unknown bias in the ocean L-band GMF model [3.3].
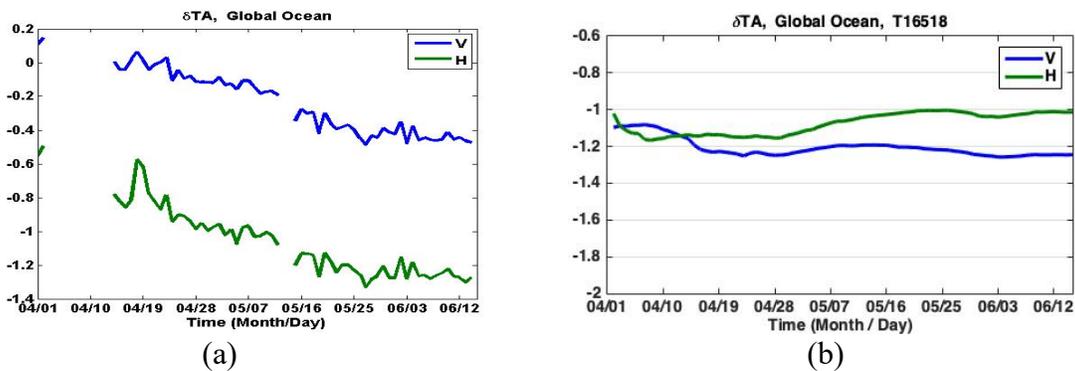

(a)   (b)

Figure 3.1 Radiometer T_A bias and drift. The unit of y-axis is Kelvin. (a) before correction; (b) after correction. Biases in δT_A are matched to the biases during SAR-off era.

The calibration drift over the the global ocean for the first 4 years and 2 months are shown in Figure 3.2 where Figure 3.2a is with descending and ascending data averaged together and Figure 3.2b is with them separate. The observed variations are most likely due to uncertainty in the ancillary data which are used for expected TA computation. The overall long-term calibration drifts in Figure 3.2a are 0.005 K/year for V-pol and 0.020 K/year for H-pol. For descending orbits in Figure 3.2b, the long-term calibration drifts are 0.002 K/year for V-pol and 0.024 K/year for H-pol, while for ascending orbits, the long-term calibration drifts are 0.010 K/year for V-pol and 0.016 K/year for H-pol.
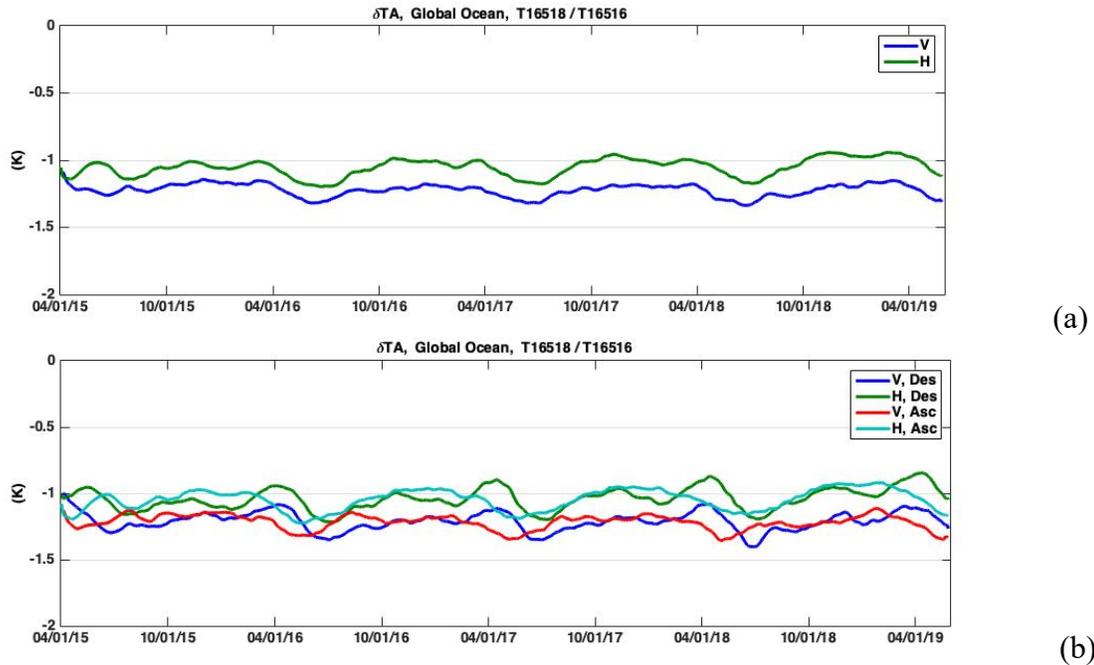
Figure 3.2 Radiometer drift over global ocean. (a) Ascending and descending data combined; (b) Ascending and descending data separated.

References

[3.1] J. Peng *et al*., "Soil Moisture Active/Passive L-Band Microwave Radiometer Postlaunch Calibration," in *IEEE Transactions on Geoscience and Remote Sensing*, vol. 55, no. 9, pp. 5339-5354, Sept. 2017. doi: 10.1109/TGRS.2017.2705342.

[3.2] J. Peng *et al*., " Soil Moisture ActivePassive SMAP Lband Microwave Radiometer PostLaunch Calibration Upgrade," *IEEE J. Sel. Topics Appl. Earth Obs. Remote Sens*., vol. 12, no. 6, pp. 1647-1657, June 2019. doi: 10.1109/JSTARS.2019.2902492, 2019.

[3.3] S.H. Yueh, W. Tang, A.G. Fore, G. Neumann, A. Hayashi, A. Freedman, J. Chaubell, and G.S.E. Lagerloef, "L-Band Passive and Active Microwave Geophysical Model Functions of Ocean Surface Winds and Applications to Aquarius Retrieval," *IEEE Trans. Geosc. Remote Sens.,* vol. 51, no. 9, pp. 4619-4632, 2013.

4   Front-End Loss Effects

4.1   Thermal Stability: Front-end RF Components and SAR Transmitter

Figure 4.1(a) below shows the RF element temperatures during a planned bake-out. Before bake-out the SAR transmitter was also turned off. The global δT_A (Fig. 4.1(b)) over the ocean shows two separate impacts due to these events.

1. A rise in the measured T_A with respect to the modeled T_A when the RF bake-out was occurring.
2. A drop in the measured T_A with respect to the modeled T_A when the SAR transmitter was turned off.
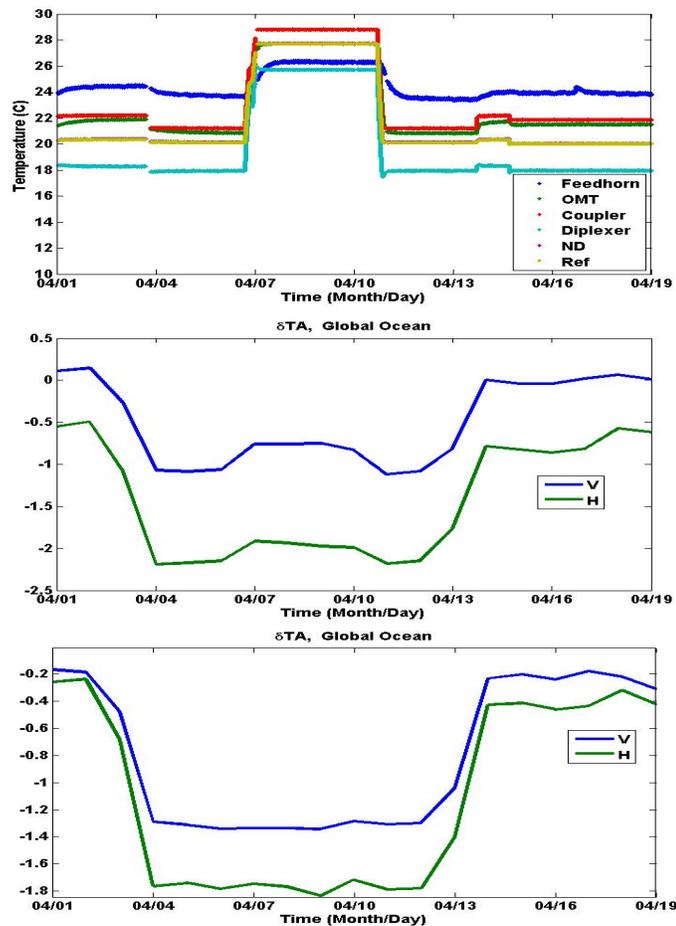

Figure 4.1: (a) Front-end temperature of the RF components over the same period. (b) Daily averaged global ocean δT_A indicating T_A biases due to SAR transmitter being turned off (Apr 3) and on (Apr 13) and radiometer bake-out (Apr 6 to Apr 10). (c) Daily averaged global ocean δTA indicating TA biases due to SAR transmitter being turned off (April 3, 2015) and on (April 13, 2015) after the adjustment of the RF front-end thermal coefficients.

The first front-end impact observed from Figure 4.1 is the change in T_A bias with change in the RF temperature components during Apr 03~13,2015. Thermal coefficients to the RF front-end

parts are finely tuned to compensate the impact of this event. The result of this update is shown in Figure 4.1(c), and it shows that the front-end thermal calibration coefficients can completely compensate for the changing thermal environment of the RF components.

The second front-end impact observed from Figure 4.1 is T_A bias due to the SAR transmitter being turned off and it is an expected occurrence from pre-launch data analysis. On July 07, 2015 (not shown in figure), the SAR transmitter encountered an anomaly that turned off the radar, causing a shift in radiometer calibration. Considering that the front-end thermal calibration coefficients can completely comensate for the thermal environment changes during bake-out period and the thermal environment changes is larger than the thermal environment change when SAR transmitter being turned on/off, the cause to the T_A bias should be unwanted signal from the SAR when the SAR transmitter is on. Therefore, the version 5 release data compensates for this T_A bias as an input bias by adjusting the Trefl_offset values prior to July 07, 2015 to account for the offset bias. The result of this update is shown in Figure 3.2.

4.2   Reflector Emissivity Model Update

The reflector physical temperature prediction used in Version 5 release data is the same as that used in Version 4 release data [4.1]. The reflector loss factor (converted from emissivity) has been changed compared to the previous version. The reflector loss factor was retrieved concurrently with the other calibration parameters with the excess correction for the reflector loss factor to be the same. The excess correction is 1.004 and it results in the reflector loss factor 1.0067 for V-pol and 1.0061 for H-pol.

Reference
[4.1] J. Peng *et al*., " SMAP Radiometer Brightness Temperature Calibration for the L1B_TB, L1C_TB (Version 4), and L1C_TB_E (Version 2) Data Products," SMAP Project, Jet Propulsion Laboratory, Pasadena, CA. June 6, 2018. [Online.] https://nsidc.org/data/smap/data_versions.

5   Full Dynamic Range Calibration

5.1   Nominal CSC to Assess Radiometer Bias and Temporal Stability

The average differences between observed and modeled T_A over the cold sky (CS) for V- and H-pol are used for assess the radiometer calibration drift and bias over CS including both the nominal Cold Sky Calibration (CSC) and the Special CSC in Section 5.2. The results are shown in Figure 5.1. The magnitude of the dips during eclipse seasons of 2017 ~2019 in release version 4 [5.1] has been reduced, and the uncertainty is not larger than 0.11 K for both V- and H-pols.
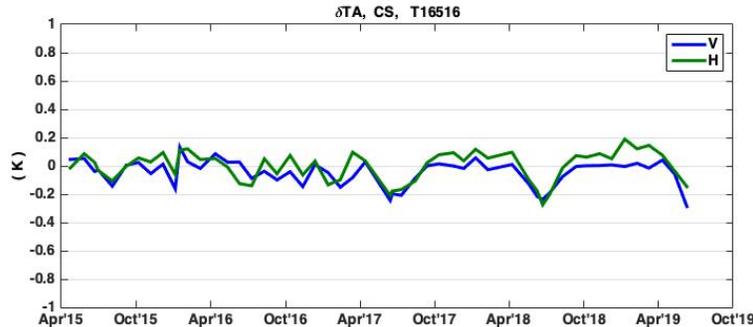

Figure 5.1. Difference between SMAP observed and modeled T_A over the cold sky for (blue) V-pol, (green) H-pol.

5.2   Special Nadir Maneuver to Assess Radiometer Bias and Temporal Stability

A special nadir maneuver (35.5° pitch angle) has been performed and the nadir-looking footprints are shown in Figure 5.2. For each nadir-looking, the TB difference between V- and H-polarizations is expected to be close to zero at nadir. Because the antenna is still scanning, strictly nadir-looking measurements are limited. To obtain more samples, the range of the nadir-looking measurement is extended to ±5 degrees of nadir pointing.

Comparison of V- and H-polarizations is performed at TA level because TB value is not available at non-science mode (e.g. Nadir-looking). With the calibration coefficients for Version 5 date release applied to Half orbit 13574_A, the δT_A difference between V- and H-polarizations are -0.10 K over land and -0.47 K over ocean. The relatively larger difference over ocean might due to the bias in the the L-band GMF model [3.3].
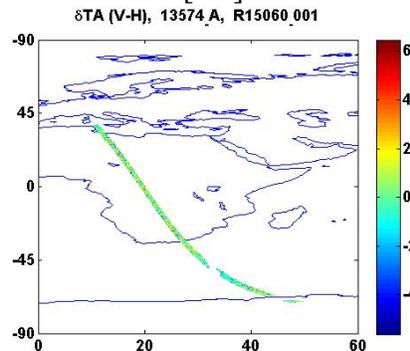

Figure 5.2 Nadir looking footprints over both ocean and Africa

14

5.3 Comparison with SMOS

SMOS and SMAP have an equatorial overpass time of 6 AM (SMOS-ascending; SMAP-descending). In order to minimize inter-comparison errors associated with temporal changes in soil moisture and temperature, a maximum time window between the two satellite observations of 30 min was allowed. Both SMAP and SMOS have an average 3-db footprint size of 40 km. Spatial variations in the contributing area were minimized by only using observations when the footprint distance was less than 1 km between SMAP and SMOS. Brightness temperatures at the top of the atmosphere (TOA) were used in the inter-comparison. This analysis was done for both the horizontal (H) and vertical (V) polarizations. Microwave observations from the SMOS mission were reprocessed to approximate SMAP microwave radiometer observations made at a constant incidence angle of 40º. Only the alias free portions of the SMOS field-of-view were used in the comparison. Additionally, the alias free portions of the swath provide brightness temperatures with the lowest NEΔT. SMOS data version v620 was used for the analysis.

This comparison was done with SMAP data version T16516. Figure 5.3 (a-b) shows the SMAP and SMOS observations over land for three years worth of SMAP data. Statistical analysis results are summarized in Table 5.1. The SMAP brightness temperatures show a very strong correlation with the SMOS observations. Some of the scatter in the inter-comparison is likely due to the presence of RFI in either or both of the SMAP or SMOS observations. Land surface heterogeneity of the footprint can also result in some scatter. The SMAP brightness temperatures at H- and V-polarizations are cooler than SMOS brightness temperature observations. The V-polarization values are relatively cooler than the H-polarization observations (relative to SMOS). The comparison between SMAP and SMOS brightness temperature shows a strong linear relationship.

Table 5.1. Summary statistics of the brightness temperature comparison between SMOS (version 620) and SMAP (T16516)

		RMSD (K)	R	Bias [SMAP-SMOS] (K)	ubRMSD (K)
H pol	Land	3.56	0.9902	**-0.90**	3.45
	Ocean	2.18	0.8522	-0.46	2.14
	Overall	2.60	0.9994	-0.57	2.53
V pol	Land	3.81	0.9903	**-2.37**	2.98
	Ocean	2.55	0.6967	-1.59	2.00
	Overall	2.92	0.9994	-0.46	2.31

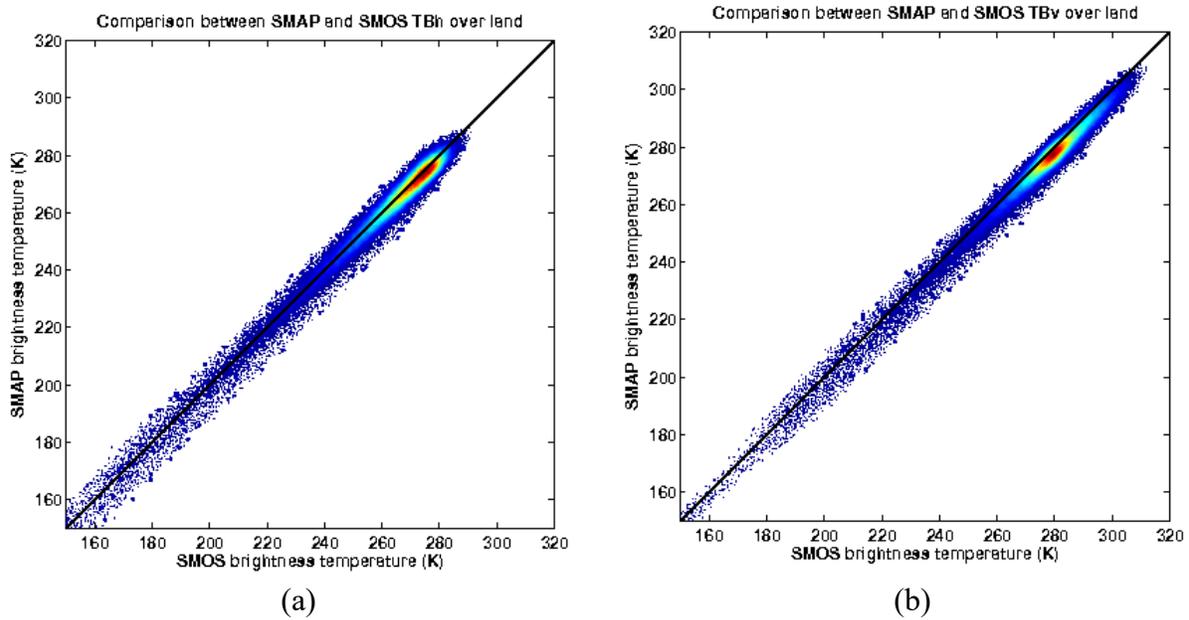(a)   (b)

Figure 5.3. Density plot of the comparison between SMAP T_B and SMOS T_B over land for (a) H-pol, and (b) V-pol. Scale adjusted for land T_B.

5.4   Comparison with Aquarius

The comparisons in surface TB between SMAP and Aquarius middle beam have been updated to the latest version of products: Aquarius 'final' version 5.0 and SMAP version 5. The difference in incidence angle between Aquarius middle beam (38.5°) and SMAP (40°) has been accounted for over ocean using 2 different methods with similar results: 1) Using radiative transfer model [6.2] and 2) incidence angle dependence empirically derived from Aquarius observations from its three beams. This result in a change to Aquarius middle beam TB by +1.85 K and -1.25 K in vertical and horizontal polarization respectively. Observations with large reflected galaxy have been filtered out.

Table 5.2 reports average differences SMAP – Aquarius (middle beam). SMAP TB are always colder than Aquarius', by ~1.1 K over ocean at both polarizations and by ~3.4 K over land. The land comparison does not include any compensation for the difference in incidence angle.

Table 5.2: Average (median) difference in TB from SMAP and
Aquarius collocations over ocean and land for May 2015.

	Ocean (no correction)	Ocean (incidence angle corrected)	Land
ΔT_v (K)	+0.70	-1.15	-3.28
ΔT_h (K)	-2.31	-1.09	-3.41

Reference

[6.1] T. Meissner et al, "The emission and scattering of L-band microwave radiation from rough ocean surfaces and wind speed measurements from Aquarius," *J. Geophys. Res. Oceans,* vol. 119, 2014. doi:10.1002/2014JC009837

[6.2] E. P. Dinnat *et al.,* "Issues concerning the sea emissivity modeling at L band for retrieving surface salinity, " Radio Sci., vol. 38, no. 4, pp. 25-1–25-4, Aug. 2003.

6   Faraday Rotation Correction Assessment

Faraday rotation is a change in the polarization of radiation as it propagates from the surface through the ionosphere to the sensor. The amount of polarization rotation depends on frequency, and at L-band (1.4 GHz) it can be on the order of 8-10 degrees even in conditions of low total electron content [6.3]. This rotation of the polarization vector is important for remote sensing because radiation emitted from the surface at one polarization (e.g. horizontal) arrives at the satellite as a combination of horizontal and vertical polarization, and retrieval algorithms such as the "single channel algorithm" used for retrieval of soil moisture are dependent on the polarization. This is a particular problem for a conical scanner such as SMAP because the variation of the rotation angle with position around the scan is of the same order of magnitude as the change with geographic position as the sensor travels in its orbit around the globe [6.1,6.2].

Because of Faraday rotation, each of the recent L-band missions in space, SMOS, Aquarius and SMAP, have included measurement of the third Stokes parameter to provide an in-situ estimate of the angle of rotation [6.5]. Aquarius demonstrated that the ratio of the third and second Stokes parameter could be used successfully to measure the rotation angle over oceans. The conical scan of SMAP and the need to operate over land for retrieval of soil moisture complicates the retrieval. The conical scan results in a rapid change of the viewing angle with respect to the local Earth magnetic field resulting in a significant change in the polarization rotation with scan angle [6.2]; and issues such as vegetation canopy and inhomogeneity of the scene over land lead to increased noise in the retrieved rotation angle [6.2,6.3].

An assessment has been conducted to determine the magnitude of the problem of retrieving the rotation angle over land and to gain insight in to the optimum approach for treating Faraday rotation in the context of remote sensing of soil moisture with a conical scanner like SMAP. Among the conclusions are:

- Spurious T3 is a problem over land;
- The retrieval of the Faraday rotation angle over is noisy (compared to the retrieval over ocean) and fails over dense vegetation where $Q = Tv - Th \approx 0$;
- Alternative approaches might improve the retrieval over land;
- Comparison of the TEC retrieved from SMAP and Aquarius suggests reasonable calibration of SMAP T3 and a functioning retrieval algorithm for Faraday rotation [7.4].

Correcting for Faraday rotation can be done in the ideal case (perfect antenna) using conservation equations for the Stokes parameters:

$$I_{toa} \quad = \quad I_{toi}$$

$$Q_{toa} \quad = \quad (Q^2_{toi} + T^2_{3,toi})^{1/2}$$

This helps avoid singularities that amplify noise when $Q \approx 0$, but does not avoid effects of spurious T_3 associated with inhomogeneous scenes.

References:

[6.1] D.M. Le Vine and S. Abraham, "Faraday Rotation with the SMAP Radiometer", MicroRad2016, Helsinki, FI, April 11-14, 2016.

[6.2] D. M. Le Vine, S. Abraham and J. Peng, "Faraday Rotation Correction for the SMAP Radiometer", IEEE Transactions Geoscience and Remote Sensing, Vol 54(4), pp 2070-2081, April, 2016, DOI: 10:1109/TGRS2015.2495168.

[6.3]D.M. Le Vine and S. Abraham, "Faraday Rotation Correction for SMAP and Soil Moisture Retrieval", IEEE Trans. Geoscience and Remote Sensing, TGARS, Vol 56 (#2), pp 655-668, February, 2017. DOI: 10.1109/TGRS.2017.2752646.

[6.4] Y. Soldo, L. Hong, S. El-Nimri and D.M. Le Vine, "Total Electron Content Retrieved From L-Band Radiometers and Potential Improvements to the IGS Model", Radio Science, Vol 53, 2018, DOI: 10.1002/2018RS006530.

[6.5] S. H. Yueh, "Estimates of Faraday rotation with passive microwave polarimetry for microwave remote sensing of Earth surfaces," *IEEE Trans. Geosci. Remote Sens.*, vol. 38, no. 5, pp. 2434–2438, Sep. 2000.

7 Reflected Galaxy Correction Assessment

7.1 Galaxy Correction Update over Ocean

The reflected galaxy correction for ocean has been upgraded for the release Version 4 and it will continue to be used for the release Version 5. (Note: No change for land). Wind speed dependent LUTs have been developed to replace the constant LUT used in release Version 3, and it's obtained by using the difference between the SMAP radiometer measurement and the modeled T_A without reflected galaxy T_A contribution involved over open and heavy-rain-free ocean region. The differences are then normalized by the ocean reflectivity (Note: The bias in H-pol described in Section 5.2 is considered in the computation of the ocean reflectivity) for given wind speeds. Figure 7.1(a) and (b) list the LUT for wind speed 3 m/s and 7 m/s, respectively. These LUT are used for L1B_TB ocean data release Version 4, while Figure 7.1(c) lists the LUT used for L1B_TB data release Version 3 and land data release Version 4. Comparing Figure 7.1(b) and (c), the difference can be observed. In addition, the wind speed depend LUT has bias correction for 3rd and 4th Stokes.
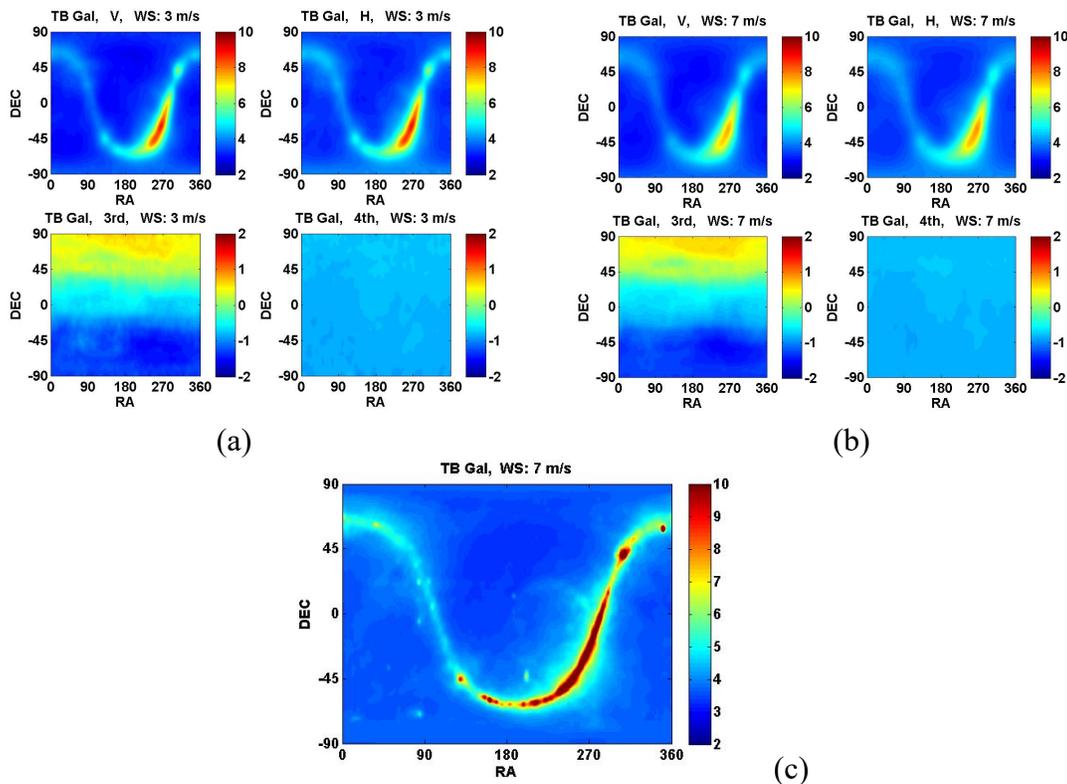

Figure 7.1 (a) LUT for wind speed 3 m/s for L1B_TB ocean data release Version 4 (b) LUT for wind speed 7 m/s for L1B_TB ocean data release Version 4 (c) LUT used for L1B_TB ocean data release Version 3 and land data release Version 4.

Comparing the ocean T_B using the upgraded reflected galaxy correction to the ocean T_B of the release version 3, the T_B change with respected to ocean wind speed is shown in Figure 7.2. The averaged difference is 0.12 K for V-pol and -0.03 K for H-pol.
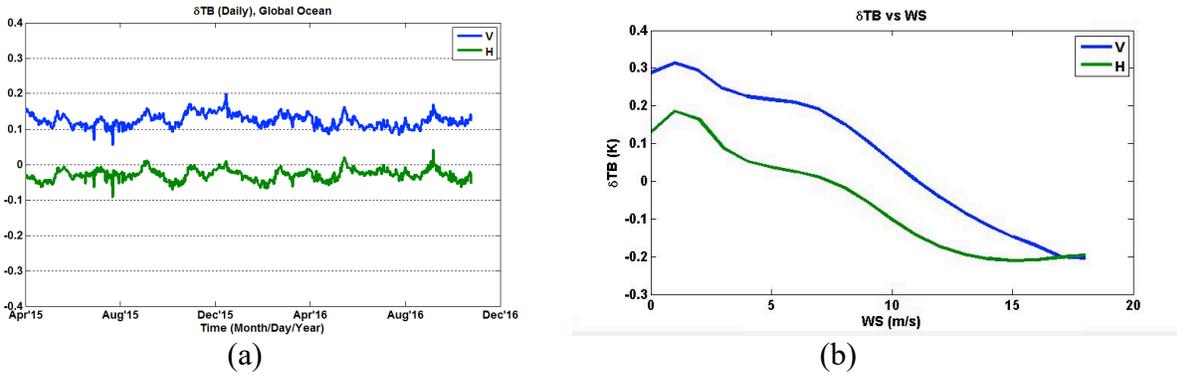
(a)   (b)

Figure 7.2   Ocean T_B difference between Version 4 and Version 3 for (blue) V-pol and (green) H-pol. (a) Daily averaged ocean T_B difference versus time. (b) Averaged ocean T_B difference versus ocean wind speeds

8 Radio-Frequency Interference Assessment

As described in [8.1] the SMAP radiometer includes a digital backend to improve the detection and filtering of radio frequency interference (RFI). The digital backend produces two independent data streams from SMAP observations (Fig. 8.1): a "fullband" product representing 32 samples of the entire observed bandwidth resolved at ∼ 300 μsec time resolution (i.e. each radar pulse repetition interval – PRI) and a "subband" product consisting of 16 frequency channels resolved in eight time samples at ∼ 1.2 msec time resolution (4 PRI's). Each of these data streams is accompanied by information on its first, second, third, and fourth integrated moments, enabling computation of the kurtosis of each as well. This information is available to ground processing for both the horizontally and vertically polarized channels and for the third and fourth Stokes parameters. As shown in Fig. 8.1, the final footprint level antenna temperature is computed in ground processing by averaging over the 8-time-by-16-channel antenna temperature spectrogram, excluding any "pixels" in the spectrogram flagged by any RFI detection algorithms. Discarding pixels from the spectrogram in the footprint integration degrades the radiometer sensitivity. The radiometer quality flag includes flags for an excessive degradation in radiometer sensitivity and an excessive detected RFI level. Additional discussion of these flags is provided in the Quality Flags section.
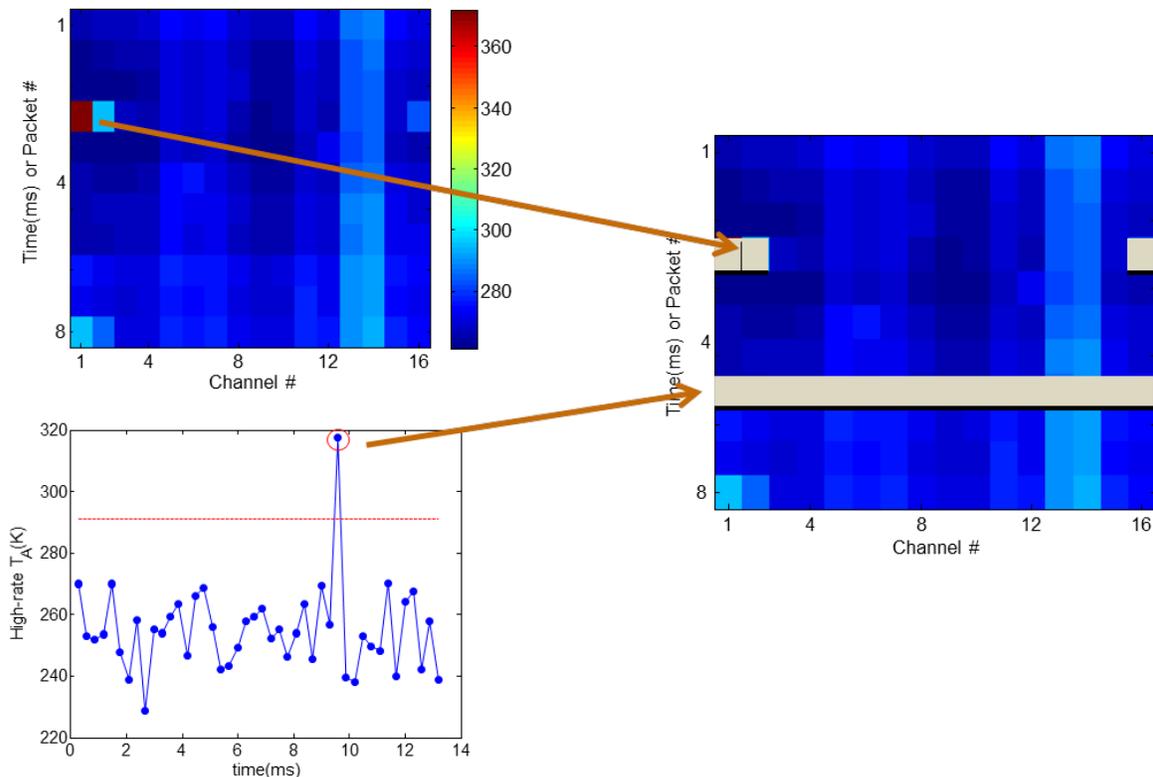

Figure 8.1: Illustration of RFI filtering process. Pixels detected in the sub-band data stream (upper left) or fullband data stream (lower left) can flag portions of the 16 channel by 8 time sample spectrogram used to compute footprint brightness temperature.

There are nine RFI detection algorithms that can flag portions of the spectrogram:

Scenario	Action
Fullband pulse detection	Flag entire "rows" in the spectrogram
Fullband kurtosis	Flag entire "rows" in the spectrogram
Fullband third Stokes	Flag entire "rows" in the spectrogram
Fullband fourth Stokes	Flag entire "rows" in the spectrogram
Subband kurtosis	Flag single pixels in the spectrogram and adjacent frequency channels
Subband third Stokes	Flag single pixels in the spectrogram
Subband fourth Stokes	Flag single pixels in the spectrogram
Subband cross-frequency	Flag single pixels in the spectrogram and adjacent frequency channels
Subband integrated cross-frequency	Flag entire "column" of spectrogram and adjacent columns

Each detection algorithm has a detection threshold setting that determines its sensitivity and false alarm rate. Detection thresholds for each detector are specified in a settings file that is resolved on a 0.1-deg-by-0.1-deg global spatial grid, distinct for ascending/descending passes and fore/aft looks. All settings are uniform in space for the kurtosis and cross frequency detection algorithms. The thresholds for the fullband pulse detector are increased (at 0.1-deg spatial resolution) for coastal regions, because the pulse detector may erroneously detect coastal crossings as RFI. The polarimetric detection thresholds (i.e. fullband or subband third or fourth Stokes detectors) have also been uniformly set with increased thresholds at coastlines for the fourth Stokes detectors.
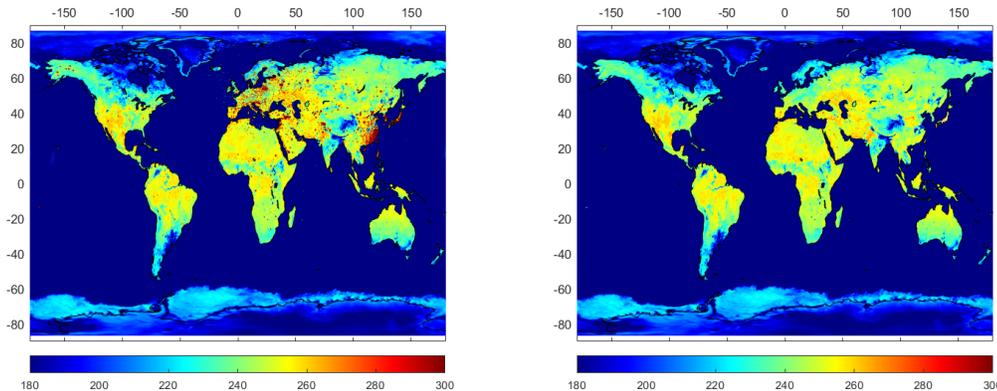

Figure 8.2: "Max hold" on a regular 0.25-deg global grid of horizontally polarized antenna temperatures , before (left) and after (right) RFI filtering, including filtered data from flags for the period March 1-8, 2020.

Because the L1B processor reports antenna temperatures both with and without RFI filtering, it is possible to determine the level of RFI detected (and removed) by SMAP. Figure 8.2 is an illustration of the "max hold" of horizontally polarized antenna temperatures compiled over the period March 1-8, 2020 on a regular 0.25-deg global grid. The "max hold" operation captured the

maximum brightness temperature that occurred over the 8-day period, and is used to illustrate strong RFI events (which are easily distinguished from the geophysical background). The left plot of Fig. 8.2 is performed using antenna temperatures with no RFI filtering, while the right is performed after RFI filtering including filtering using flagged data. The left image shows strong RFI sources (the anomalously high – or red – regions of the image) particularly in Europe and Asia. The significant differences obtained in the right image illustrate that RFI filtering is reducing RFI corruption of SMAP data. However, some strong sources remain even after RFI filtering.
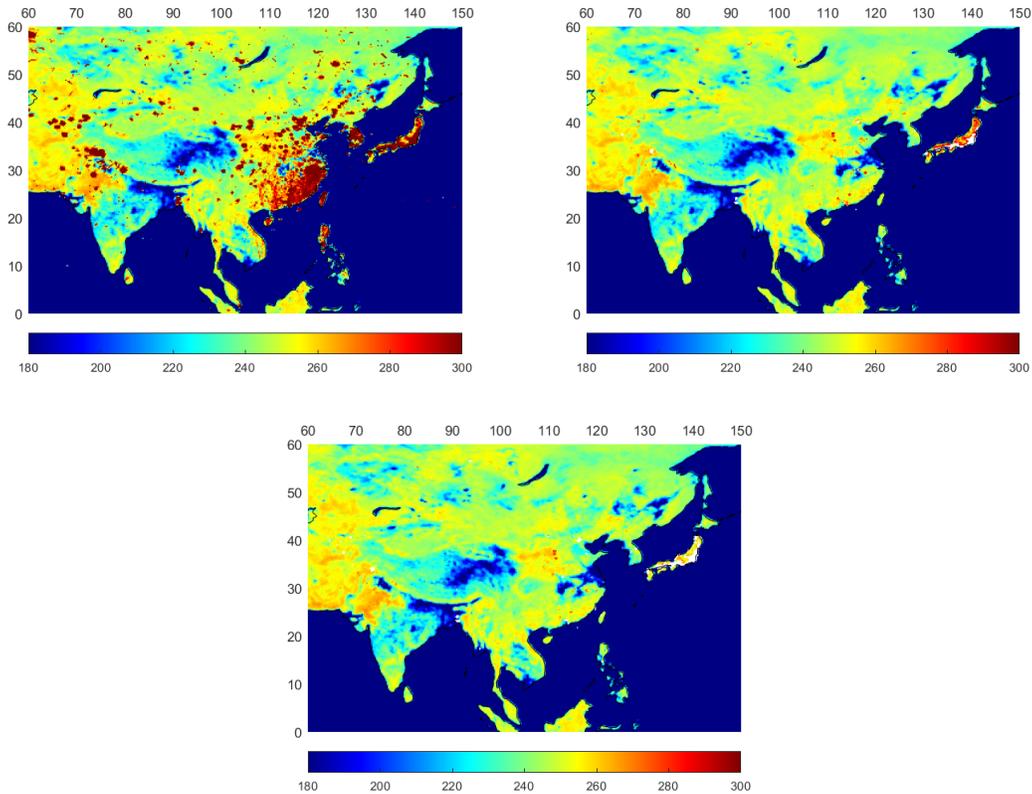

Figure 8.3: Zoom of Fig. 8.2 in Eastern Asia. (upper left) Max hold of horizontally polarized antenna temperatures prior to RFI filtering. (upper right) After RFI filtering. (lower) After RFI filtering and excluding any flagged data.

Figure 8.3 (upper left) is a zoom of Fig. 8.2 (left) in Eastern Asia; the results show strong RFI in Eastern China and over almost the entirety of Japan. The results again show significant reduction in corruption following RFI filtering (upper right), but Japan remains significantly impacted by RFI. The lower plot in Fig. 8.3 illustrates the max hold excluding any points removed by data quality flags. These flags remove much of the data over Japan, showing that data containing uncorrectable RFI is at least being excluded from further analysis in most cases. An analysis of RFI in Japan was performed in conjunction with a similar analysis by the RFI team for SMOS. The main source of the persistent RFI in Japan has been identified as related to ground satellite TV receivers that leak into the protected part of the L-Band spectrum (used by SMOS and SMAP) when improperly installed. Analyses by both the SMOS and SMAP RFI teams have confirmed that channels 19 and 21 of the Japanese TV receiver are the main cause of the large RFI sources in Japan. Reports of these sources were filed with spectrum management authorities by both the

24

SMOS and SMAP teams. Similar reports have also been produced for sources in China and in the United States.

Figure 8.4 illustrates the detected RFI levels for ascending (left) and descending (right) passes for the period 7/1-7/8/20, again as a max hold in horizontal polarization. The results confirm the strong RFI observed in Europe and Asia. In this case, the color scale is reduced from Fig. 8.1 so that lower level RFI corruption (at the level of 10K or less) can be more clearly observed. Differences between ascending and descending passes also capture variations in RFI source transmissions with time of day and azimuth angle.
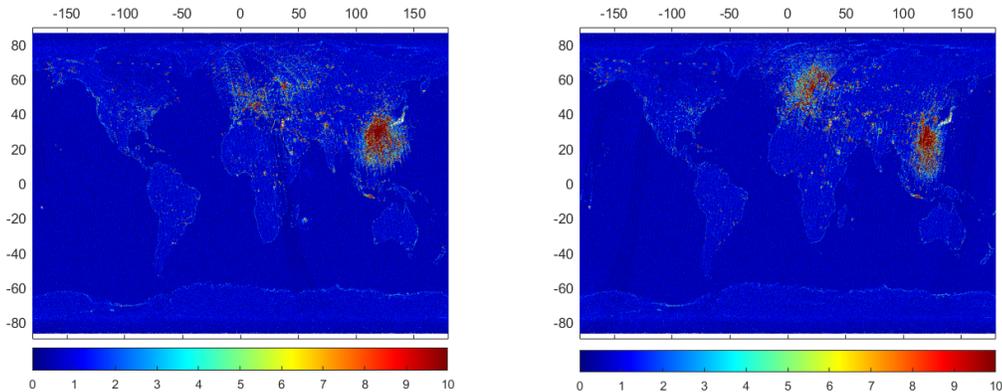

Figure 8.4: "Max hold" on a regular 0.25-deg global grid of horizontally polarized detected RFI, for ascending (left) and descending (right) passes, fore looks, for the period July 1-8, 2020.

Figure 8.5 illustrates the average fraction of the spectrogram flagged (i.e. out of 128 spectrogram pixels per footprint) on a global 0.25-deg grid. Obvious RFI sources are evident, but the ~5.5% false alarm rate of the detection algorithm is also apparent when RFI sources appear to be absent. This detection rate implies that seven spectrogram pixels are flagged on average in the absence of RFI, causing degradation in radiometer sensitivity of the square root of 128/121, or 1.3 percent.
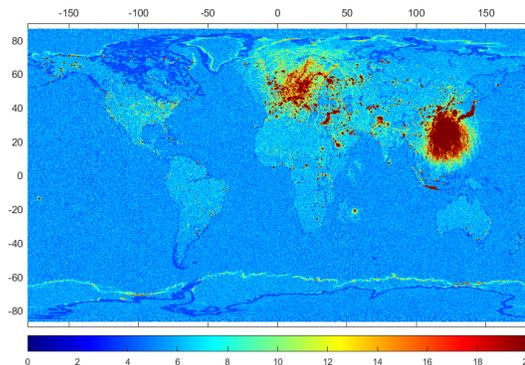

Figure 8.5: Average percentage of the 128 pixel spectrogram flagged, on a global 0.25 deg x 0.25 deg grid in horizontal polarization for the period July 1-8, 2020. The lower detection rate along the coastlines is due to the increased thresholds of the time domain (pulse) detector in these regions.

Figure 8.6 provides additional information on overall brightness temperature and RFI statistics. The upper left plot is a complementary cumulative distribution function (CCDF) of horizontally polarized antenna temperatures over July 2020, including antenna temperatures prior to filtering, after filtering, and after filtering excluding flagged data.
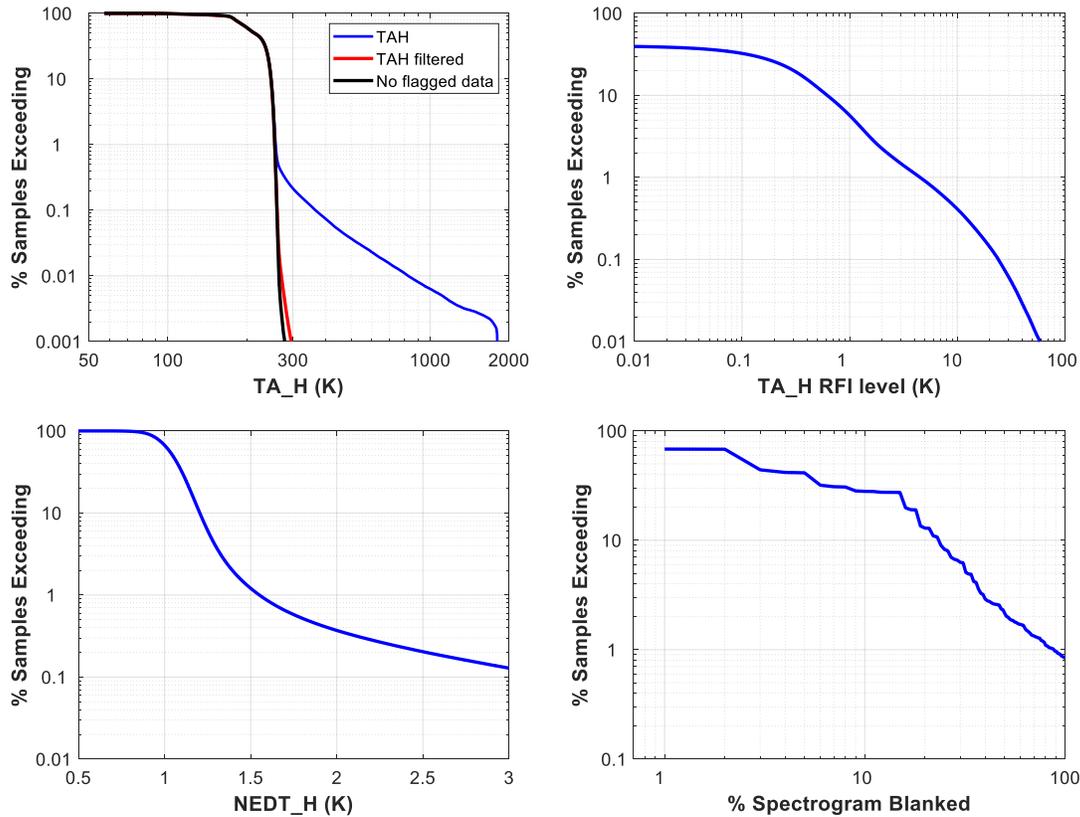

Figure 8.6: Summary statistics of SMAP horizontally polarized antenna temperatures for July 2020. (upper left) Complementary cumulative distribution function (CCDF) for antenna temperatures before RFI filtering, after RFI filtering, and after RFI filtering and flagging (upper right) CCDF of detected RFI levels (lower left) CCDF of NEDT following RFI filtering (lower right) CCDF of percentage of spectrogram flagged. Summary statistics use footprints over land only.

The results show the dramatic reduction in antenna temperatures greater than 300 K, indicating successful detection and filtering of large RFI sources. The upper right plot is a CCDF of the detected RFI level in horizontal polarization. The results show, for example, that ~ 1% of SMAP footprints are detected to have RFI levels of ~5 K or more, while ~ 6 % of SMAP footprints have a detected RFI level of 1 K or more. The lower left plot is a CCDF of the radiometer sensitivity in horizontal polarization (NEDT) following RFI filtering. Approximately 99% of SMAP footprints have an NEDT < 1.5 K, while ~ 0.4% have an NEDT > 2 K. Footprints having NEDT greater than or equal to 2 K are flagged in downstream processing (as indicated by the vertical line in the figure). Finally, the lower right plot is a CCDF of the percentage of the spectrogram flagged, and

shows that, for example, approximately 10% of SMAP footprints have 20% or more of the spectrogram flagged.

In general, the results obtained to date indicate that SMAP's digital backend and associated RFI detection and filtering algorithms are working successfully to improve the quality of SMAP brightness temperature measurements. However RFI corruption of SMAP data remains, in some cases sufficient to exclude large spatial regions from soil moisture retrieval. Beyond the results shown, SMAP's digital backend produces a wealth of additional information on the frequency, time, and kurtosis properties of global L-band RFI sources. These data are being used to continue to refine RFI processing so that future product releases will achieve further improvements.

A peer-reviewed assessment was recently published [8.2]:

References:

[8.1] Piepmeier, et al., "Radio-Frequency Interference Mitigation for the Soil Moisture Active Passive Microwave Radiometer," IEEE Transactions on Geoscience and Remote Sensing, 52(1), pp. 761-775, 2014. DOI: 10.1109/TGRS.2013.2281266

[8.2] Mohammed, et al., "SMAP L-Band Microwave Radiometer: RFI Mitigation Prelaunch Analysis and First Year On-Orbit Observations," IEEE Transactions on Geoscience and Remote Sensing, 54(10), pp. 6035 - 6047, 2016. DOI: 10.1109/TGRS.2016.2580459.

9 Water/Land Contamination Correction Assessment

In regions near the coast or near inland bodies of water, the SMAP footprint contains land and water, which results in errors in the soil moisture estimation. The mixed land and water emissions lead to an underestimation of the brightness temperature and thus an overestimation of soil moisture. Figure 9.1 displays a view of the Great Lakes. On the right, the figure shows the brightness temperature maps showing the smooth transition of the water/land interface due to land/water contamination (yellow and light blue colors). On the left is the corresponding soil moisture map. The blue rings around the lakes are caused by the water contamination. The determination of the land and water brightness temperatures contributing to the sensor measurement will not only have a significant impact on the reduction of the soil moisture errors near coastal zones but also on the retrieval of other physical parameters provided by the high level SMAP products.

We applied a single measurement algorithm, detailed in [9.1, 9.2] to separate the land and water contribution for the uncorrected SMAP measurements. The L1B_TB and L1B_TB_E products provides water contaminated corrected brightness temperature when the footprint center (or the grid point in the L1B_TB_E case) lies on land and land contaminated corrected brightness temperature when the footprint center lies on water. The temperature corrections were performed under the following rules:

1. Only if sea ice fraction was set to zero
2. Over land, water contamination correction is performed if water fraction is smaller than 0.9
3. Over water, land contamination correction is performed if water fraction is greater than 0.1

We also set some parameters to certify that the product was providing realistic temperature values when the water/land contamination correction failed to correct successfully:

1. Valid range for T_B V polarization [50K: 340K]. Values outside this range are replaced with fill values.
2. Valid range for T_B H polarization [30K: 340K]. Values outside this range are replaced with fill values.
3. Over land, if corrected T_B < uncorrected T_B then value is replaced with fill values.
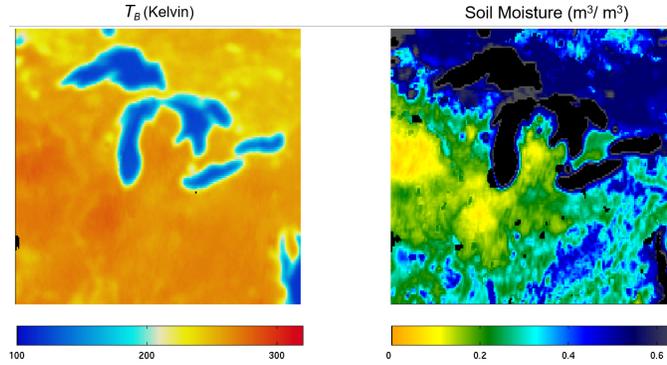4. Over water, if corrected T_B > uncorrected T_B then value is replaced with fill values

Figure 9.1. Left: Brightness temperature map of the Great Lakes showing yellow and light blue colors at the edges of the lakes caused by the land/water contamination. Right: Corresponding soil moisture map with presence of intense blue colors around the lakes due to overestimation of soil moisture.
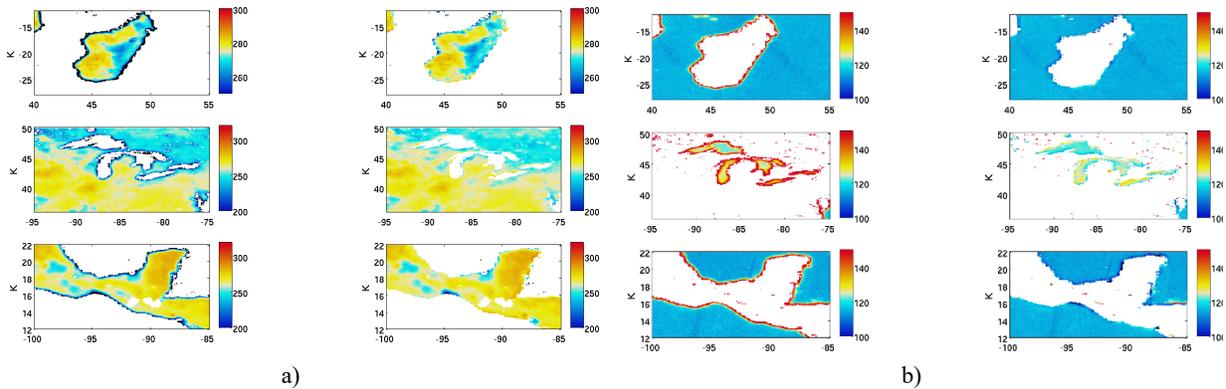

Figure 9.2. a) Results over land using real SMAP measurements. Left: uncorrected data. Right: corrected land brightness temperature

Figure 9.2. b) Results over water using real SMAP measurements. Left: uncorrected data. Right: corrected water brightness temperature.

In this report, we show the results obtained after implementation of our algorithm. Maps showing results using real data are displayed in Figure 9.2. In Figure 9.2 a) we can observe that the intense blue borders corresponding to cold temperatures in the coastal areas were removed after correction. Figure 9.2 b) shows the uncorrected and corrected brightness temperature over ocean. We can see in some areas that the corrected brightness temperatures over ocean are underestimated. We suspect that residual pointing errors maybe the cause of those anomalies as well as inaccurate estimation of land brightness temperature. Figure 9.3 a) and b) display scatter plots of T_B as a function of water fraction before and after correction for the different regions. It can be observed that after correction all dependence on water fraction was eliminated. In Figure 9.4 we display the mean and standard deviation (Std) of differences between TB after and before correction for land and water brightness temperature. Figure 9.4 provides an idea of the expected correction values as a function of water fraction and the expected uncertainty. It is important to remark that the contributors to the uncertainty are not only errors in the water

29

correction algorithm (uncertainties in water fraction, NEDT, T_B water (or land) estimation, …) but also in land type variations, urban areas, and vegetation among others.
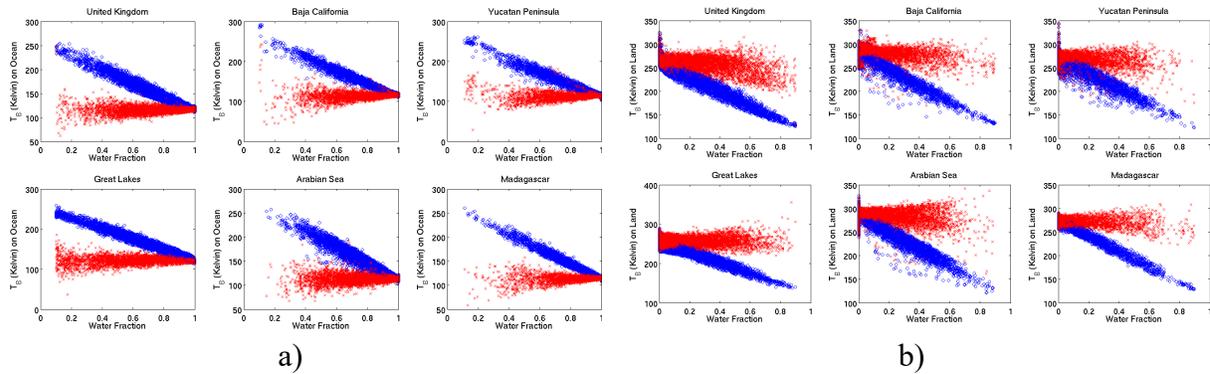

a)

b)

Figure 9.3. a) Scattering plot of uncorrected T_B (blue circles) and corrected land T_B (red times) as a function of Water fraction. From left to right; Top: United Kingdom, Baja California and Yucatan Peninsula; Right: Great Lakes, Arabian Sea and Madagascar. Before correction the T_B decreases with land fraction and after correction, we remove that dependence.

Figure 9.3. b) Scattering plot of uncorrected T_B (blue circles) and corrected water T_B (red times) as a function of Water fraction. From left to right; Top: United Kingdom, Baja California and Yucatan Peninsula; Right: Great Lakes, Arabian Sea and Madagascar. Before correction the T_B decreases with land fraction and after correction, we remove that dependence.
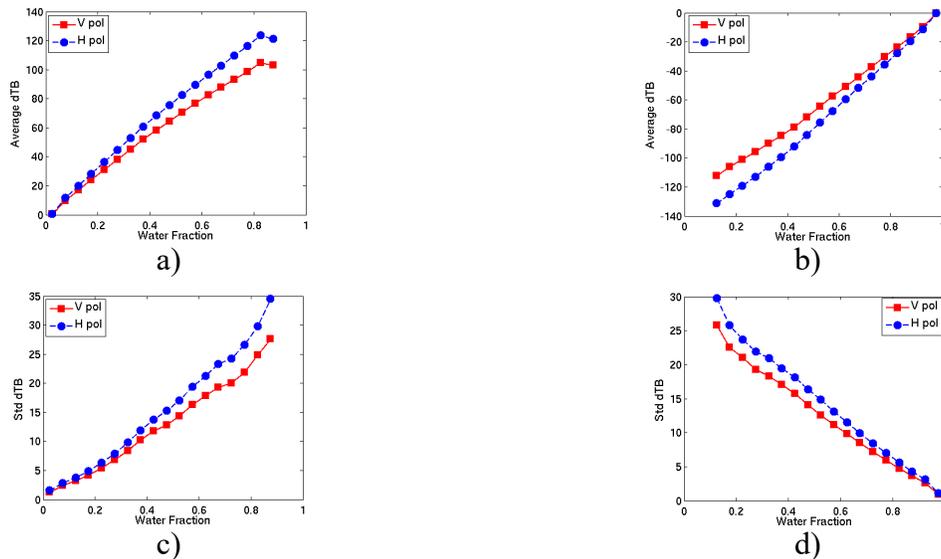

a)

b)

c)

d)

Figure 9.4. Mean (a) and Std (c) of the differences corrected land T_B – uncorrected land T_B as a funtion of water fraction. Expected errors as function of water fraction.

Figure 9.4. Mean (b) and Std (d) of the differences corrected water T_B – uncorrected water T_B as a funtion of water fraction. Expected errors as a function of water fraction.

References:

[9.1] SMAP L1B_TB Algorithm Theoretical Basis Document – Online
(https://nsidc.org/sites/nsidc.org/files/files/278_L1B_TB_RevA_web.pdf)

[9.2] SMAP L1B_TBE Algorithm Theoretical Basis Document – Online
(https://nsidc.org/sites/nsidc.org/files/technical-
references/SMAP_L1B_TB_E_Product_ATBD_D-56287.pdf)

10 Fore and Aft Differences

This section discusses the comparison of geolocated temperature (antenna or brightness). The radiometric data are subdivided into ascending/descending orbits and into forward/backward looks. The data used represent one SMAP period of observations (8 calendar days) from 00:41:38 on May 3, 2015 to 00:41:51 on May 11, 2015. The data were first gridded on a regular 0.25-deg grid. For each pixel, the average, root-mean-squared, and the number of weighted 'hits' of the radiometric data were calculated. For a grid of spacing Q, the average signal T at each pixel (x,y) is given by:

$$T(x, y) = \frac{\sum_i T_i * W_i}{\sum_i W_i}$$

where T_i is the (antenna/brightness) temperature of the i-th footprint, the weight factors are given by:

$$W_i = \frac{1/d_i}{\sum_i 1/d_i}$$

In this analysis, the following definition of d_i was adopted:

$$d_i \begin{cases} = \sqrt{(lat_i - y)^2 + (lon_i - x)^2} & \text{when } |(lat_i - y)| < Q \text{ and } |(lon_i - y)| < Q \\ = 0 \text{ elsewhere} \end{cases}$$

where the sum over i includes all available footprints.

When binning is done on a 0.25-deg grid, there are ~ 1.0e6 possible grid points over the Earth. Since each half-orbit file contains ~ 1.5e5 unique footprints, one full period of SMAP data (8 calendar days) produces > 15 'observations' of each grid point. In this time frame we observed these anomalies:

1) File 1349_D is missing ~90% of the expected data
2) File 1404_D lost a few scans over North America
3) File 1442_D is missing ~75% of the expected data

The robustness of the analysis was tested by creating, from the reported geolocation information, a corresponding set of control orbits. In these orbits, the radiometric data field is replaced by a number which represents the integration of a digital water fraction map (resolution 0.01 deg) with an elliptical Gaussian beam of the same HPBW as the SMAP's antenna; an ocean footprint has value of 1. The test-file reproduces all imperfections of L1B geometry information, but none of the (possible) inaccuracies from Solar/Lunar/Galactic/atmospheric/APC/Faraday corrections.

Fig. 10.1 shows the coverage map of the number of hits for a representative orbital geometry (descending orbits and fore looks), and the difference in the coverage for this and the corresponding combination (descending orbits and aft looks).
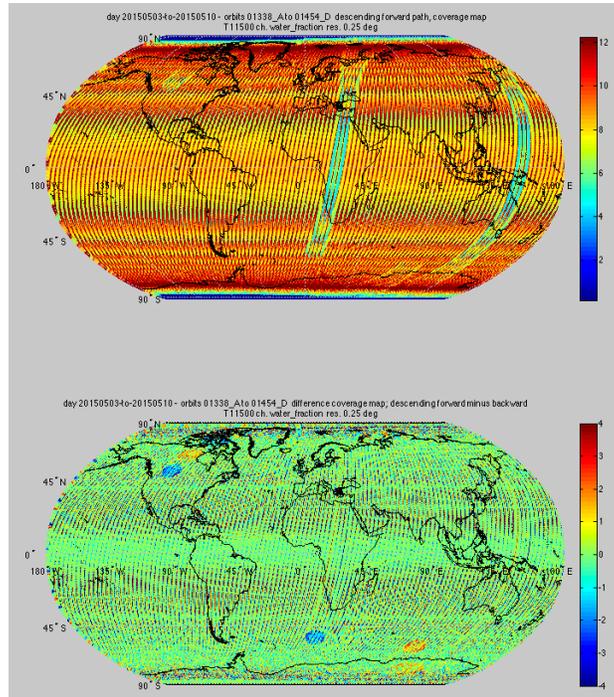

Figure 10.1: The number of hits for a representative orbital geometry over a 0.25-deg grid. Abnormal coverages over North America, the southern oceans and Antarctica were the results of the data anomalies (missing/incomplete files) listed in the text.
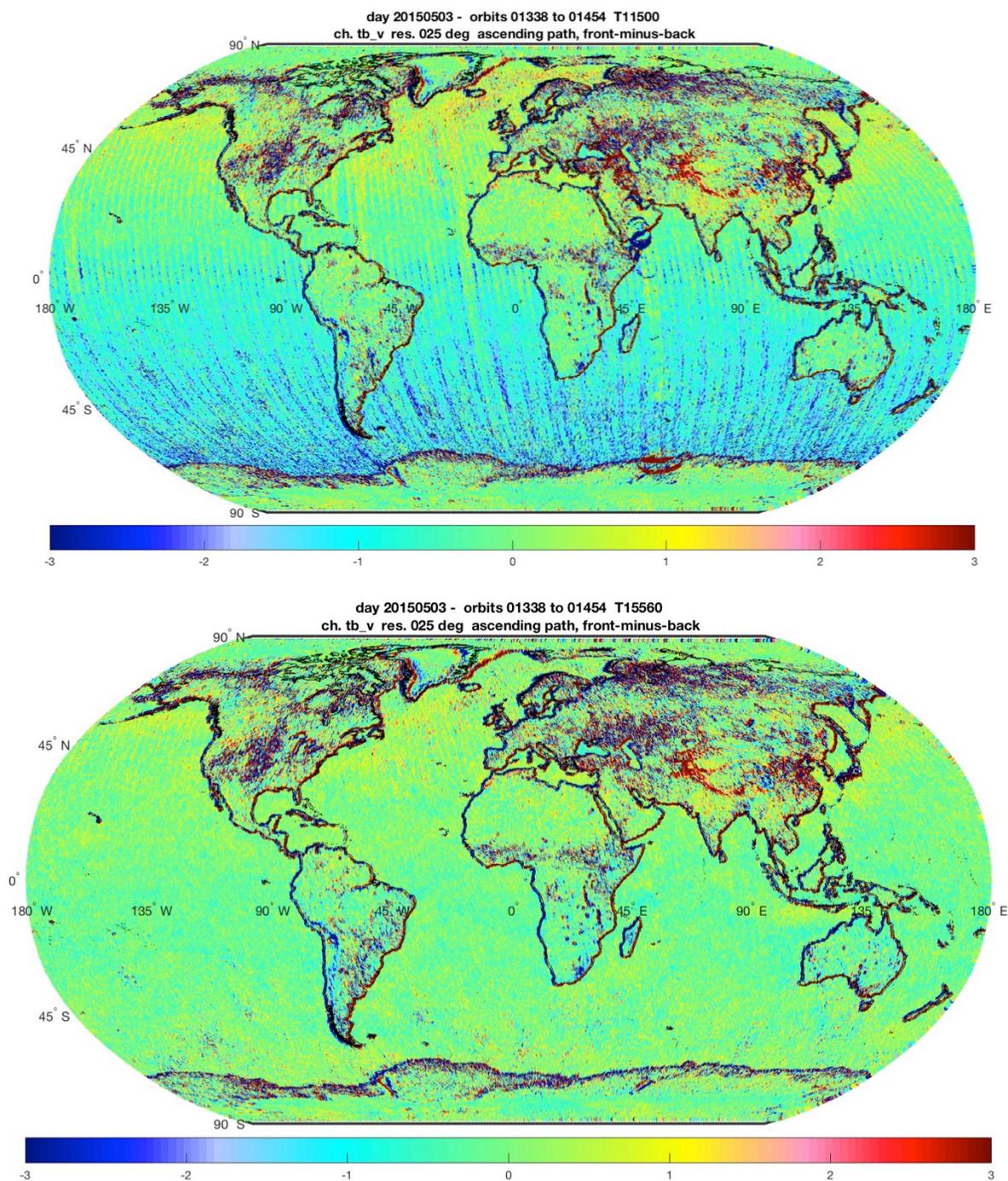
Figure 10.2 – Results from the front-back analysis applied to data from the Version 3 data (top) and Version 4 data (bottom) for V-pol ascending orbits.

Although Figure 10.2 shows data only for the V-pol ascending orbits, the results shown therein are representative of the descending orbits and of the other polarizations. Striping over the ocean, which is evident in the version 3 data processed, is absent under the version 4 data.

Still unsolved is the coastlines' consistent, repeatable, predictable colorization, which we attribute to asymmetry in the antenna sidelobe levels. It is these coastline pixels which drive the wings of the distribution, as shown in Figure 10.3.
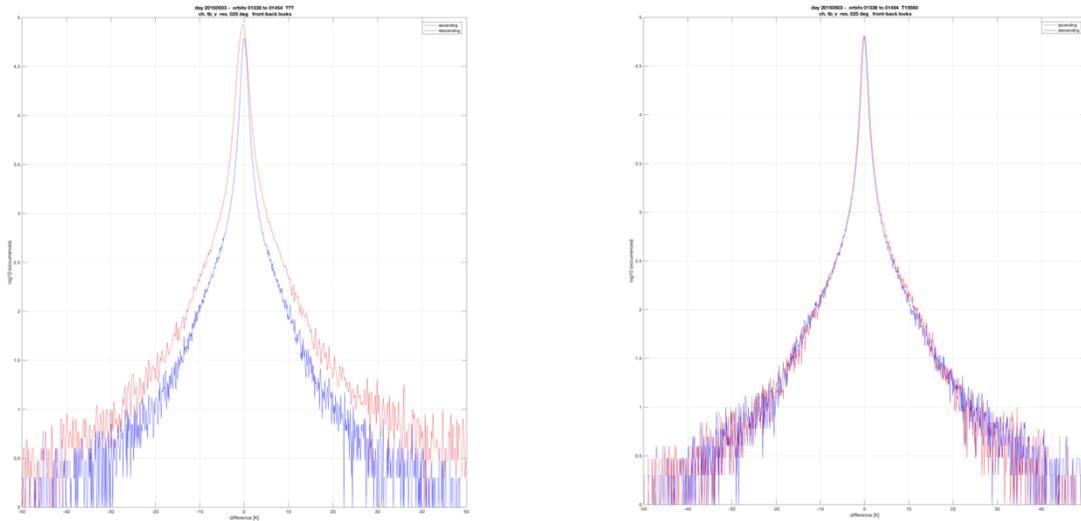

Figure 10.3 – Distributions of the differences between front and back for ascending (red) and descending (blue) orbits under the old (left side) and new (right side) code.

11 Quality Flags

11.1 Implementation and Purpose

The full design of the L1B product is described in the SMAP Level 1B Radiometer (L1B_TB) Product Specification Document (SMAP Project, JPL D-72552, Jet Propulsion Laboratory, Pasadena, CA).

There are four quality flag data fields in the L1B product, one for each channel. These data fields are encoded in two-byte integers that, upon conversion into the respective 16-bit binary representations, indicate the effectiveness (or lack of it) of post-measurement correction performed to the antenna temperatures acquired by the radiometer. All four quality flags follow the same convention of bit usage:

- 0: A favorable condition was met in L1B TB processing
- 1: A favorable condition was not met in L1B TB processing

In addition, a '0' in the master bit (the least significant bit) indicates that a given TB sample is deemed to have acceptable quality. Table 11.1 lists the threshold values for key bit flags A summary definition of these quality flags is on the next page in Table 11.2.

Table 11.1: Threshold values for key bit flags in L1B_TB

Bit	Flag Name	Criterion	Threshold(s)	Units
1	Range flag	within	[0,335]	K
2	RFI detection flag	>	2	K
4	NEDT flag	>	2	K (rms)
5	Direct sun correction	>	200	sfu
6	Reflected sun correction	>	200	sfu
7	Reflected moon correction	≤	3	deg
9	Reflected galaxy correction	>	5	K

Note: The quality flag "Reflected sun correction" in bit 6 also rejects data using the rule:

Brightness_Temperature.solar_specular_theta < 15

The user is encouraged to add an additional filter when using the data for **oceanographic** purposes. This condition should be used to *ignore* data:

Brightness_Temperature.solar_specular_theta < 50

Table 11.2: Design of L1B_TB quality flag

Bit	Bit Definition	Interpretation
0	Quality	0: Brightness temperature measurement has acceptable quality. 1: Use of brightness temperature not recommended.
1	Range	0: Brightness temperature measurement falls in expected range. 1: Brightness temperature value is out of range.
2	RFI detection	0: RFI not detected. 1: RFI detected.
3	RFI correction	0: Either RFI was not detected, or the algorithm that removes RFI operated successfully. 1: If RFI was detected, the software was unable to correct the brightness temperature for RFI.
4	NEDT correction	0: Brightness temperature measurement has acceptable NEDT. 1: Use of Brightness temperature not recommended, since NEDT exceeds pre-determined threshold.
5	Direct sun correction	0: Correction for direct sun operated successfully on the brightness temperature. 1: Correction for direct sun did not function or yielded poor results on the brightness temperature.
6	Reflected sun correction	0: Correction for reflected sun operated successfully on the brightness temperature. 1: Correction for reflected sun did not function or yielded poor results on the brightness temperature.
7	Reflected moon correction	0: Correction for reflected moon operated successfully on the brightness temperature. 1: Correction for reflected moon did not function or yielded poor results on the brightness temperature
8	Direct galaxy correction	0: Correction for direct galaxy operated successfully on the brightness temperature 1: Correction for direct galaxy did not function or yielded poor results on the brightness temperature.
9	Reflected galaxy correction	0: Correction for reflected galaxy operated successfully on the brightness temperature. 1: Correction for reflected galaxy did not function or yielded poor results on the brightness temperature.
10	Correction for atmospheric condition	0: Correction for atmospheric conditions operated successfully on the brightness temperature. 1: Correction for atmospheric conditions did not function or yielded poor results on the brightness temperature.
11	Faraday rotation correction	0: Correction for Faraday rotation operated successfully on the brightness temperature. 1: Correction for Faraday rotation did not function or yielded poor results on the brightness temperature.
12	Null value	0: The corresponding brightness temperature element contains a calculated value. 1: The corresponding brightness temperature element is null.
13	Half orbit location	0: The corresponding brightness temperature lies within the half orbit specified in the file name. 1: The corresponding brightness temperature lies outside of the half orbit specified in the file name.
14	RFI check	0: The difference between unfiltered and RFI-filtered TA's is low enough to be acceptable. 1: The difference between unfiltered and RFI-filtered TA's is too large. The resultant brightness temperature likely remains contaminated with RFI.
15	RFI clean flag	0: The brightness temperature measure is free of RFI. 1: The brightness temperature measure is RFI contaminated.

12 L1C Gridded Products

12.1 Standard L1C_TB Product

12.1.1 Overview

The L1C TB product is derived from the L1B TB product, which represents calibrated, geolocated, time-ordered TB observations acquired by the radiometer. To generate the standard L1C product the processing software first ingests the L1B data. Based on the geometry and geolocation information, the ingested data are then re-mapped on a family of Earth-fixed grids using a gridding algorithm. The L1C data product is thus simply a gridded version of the L1B data product sharing the same major output data fields. Each product represents one half orbit, where the half-orbit boundaries are set at the southernmost and northernmost location of the spacecraft orbit path, separating ascending and descending orbit segments. Only those cells that are covered by the actual swath for a given projection are written in the product.

The L1C product presents the data in three projections at 36-km grid resolution (Section 12.2):

- Global Cylindrical projection ('M36' grid)
- North Polar projection ('N36' grid)
- South Polar projection ('S36' grid)

The projections are based on the NSIDC's EASE-Grid 2.0 specifications for SMAP [12.1]. All elements in L1C are stored as HDF5 Datasets. Each projection corresponds to a separate HDF5 Group. Within each group, the data are provided in fore-looking and aft-looking views. Each set of looks contains TB observations, instrument viewing geometry information, and quality flags. The fore-looking set refers to information derived from the L1B observations acquired in the forward-looking portion of the scans when the antenna scan angle falls between 270 deg and 90 deg; the aft-looking set refers to information derived from the L1B observations acquired in the backward-looking portion of the scans. Only those cells that are covered by the swath for a given projection are written in the product. This organization is reflected schematically in Table 12.1.

Table 12.1: Fore- and aft-look data fields are stored separately in three projection groups.

L1C_TB					
N36 North Polar EASE-Grid 2.0		M36 Global Cylindrical EASE-Grid 2.0		S36 South Polar EASE-Grid 2.0	
Fore-looking	Aft-looking	Fore-looking	Aft-looking	Fore-looking	Aft-looking
1-D Array1	1-D Array1	1-D Array1	1-D Array1	1-D Array1	1-D Array1
1-D Array2	1-D Array2	1-D Array2	1-D Array2	1-D Array2	1-D Array2
1-D Array3	1-D Array3	1-D Array3	1-D Array3	1-D Array3	1-D Array3
:	:	:	:	:	:
1-D ArrayN	1-D ArrayN	1-D ArrayN	1-D ArrayN	1-D ArrayN	1-D ArrayN

12.1.2 EASE Grid

The EASE-Grid 2.0 has a flexible formulation. By adjusting one scaling parameter it is possible to generate a family of multi-resolution grids that "nest" within one another. The nesting can be made "perfect" in that smaller grid cells can be tessellated to form larger grid cells, as shown in Fig. 12.1.
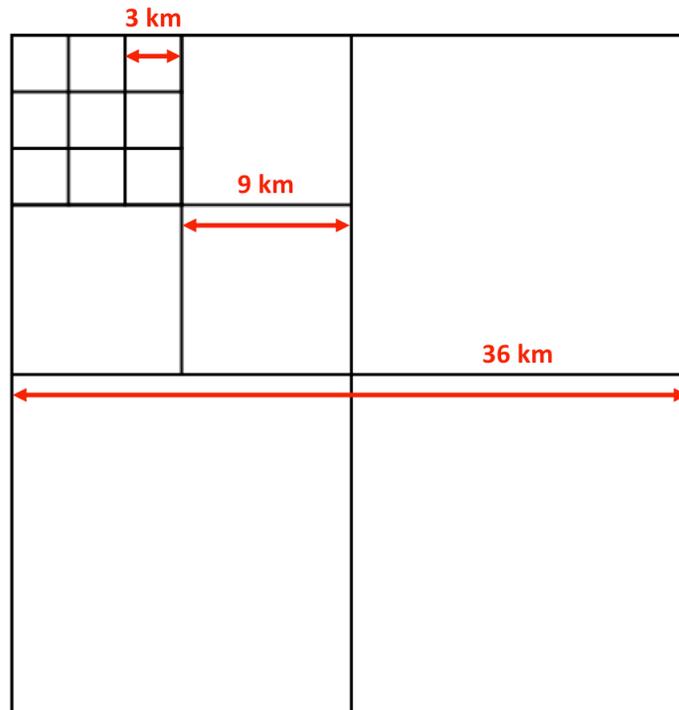

Figure 12.1: Perfect nesting in EASE-Grid 2.0 – smaller grid cells can be tessellated to form larger grid cells.

This feature of perfect nesting provides SMAP data products with a convenient common projection for both high-resolution radar observations and low-resolution radiometer observations, as well as their derived geophysical products. The three projections are illustrated in Fig. 12.2.
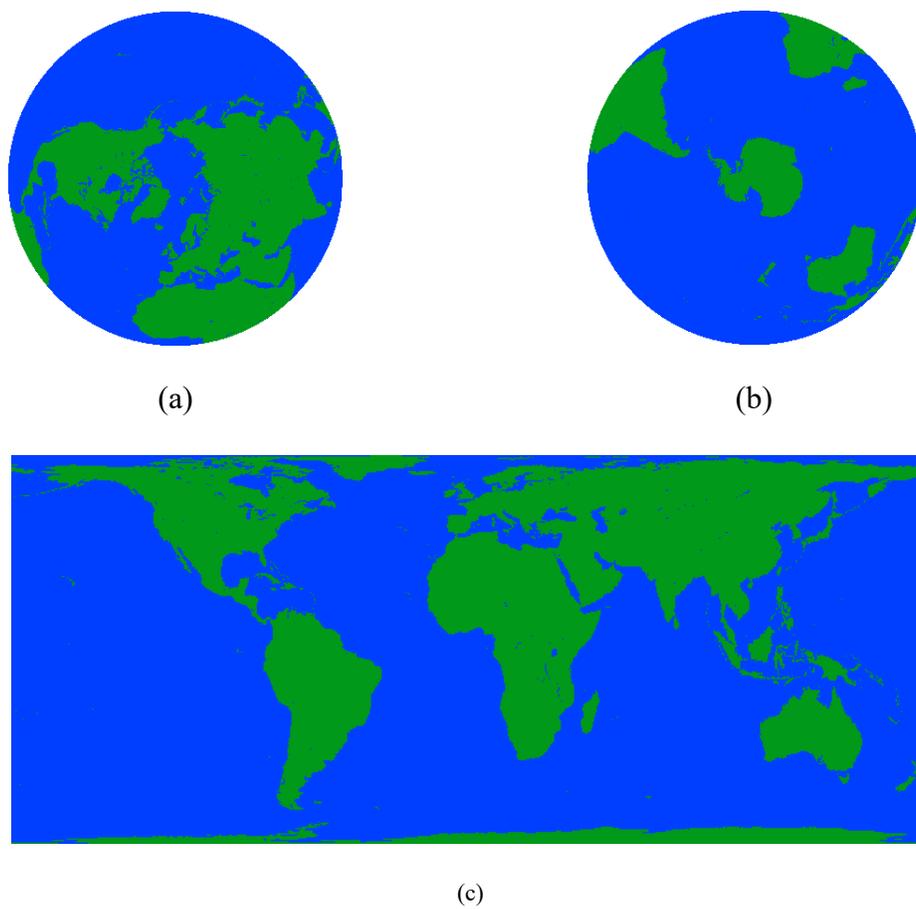

(a)   (b)

(c)

Figure 12.2: EASE-Grid 2.0 examples: (a) North Polar projection, (b) South Polar projection, and (c) Global Cylindrical projection. Figures credited to NSIDC.

12.1.3 L1C Output Fields

The L1C product inherits the majority of output fields of the L1B product. The output fields are separated into fore- and aft-looking subgroups in each EASE-2.0 Grid projection for both ascending and descending granules. Data fields are stored as one-dimensional arrays of size N, where N is the number of valid cells covered by the radiometer swath on the grid. Note that N varies with projections, but remains the same for both fore-looking and aft-looking views within a given projection. A detailed coverage of L1C data fields can be found in the Level 1C Radiometer Product Specification Document [12.2].

Figures 12.3-6 show sample L1C images on Global Cylindrical, North Polar, and South Polar EASE-Grid 2.0 projections. Fore- and aft-look data are available in the product to enable radiometric analyses over regions where there is strong TB azimuthal dependence.
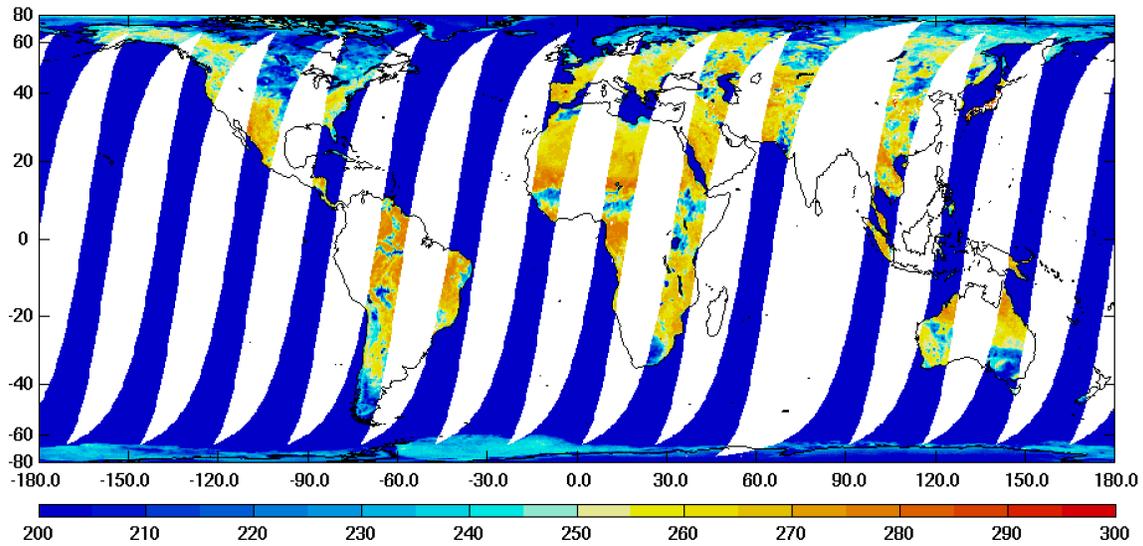
Figure 12.3: Descending fore-look H-polarized TB on Global Cylindrical EASE-Grid 2.0 projection.
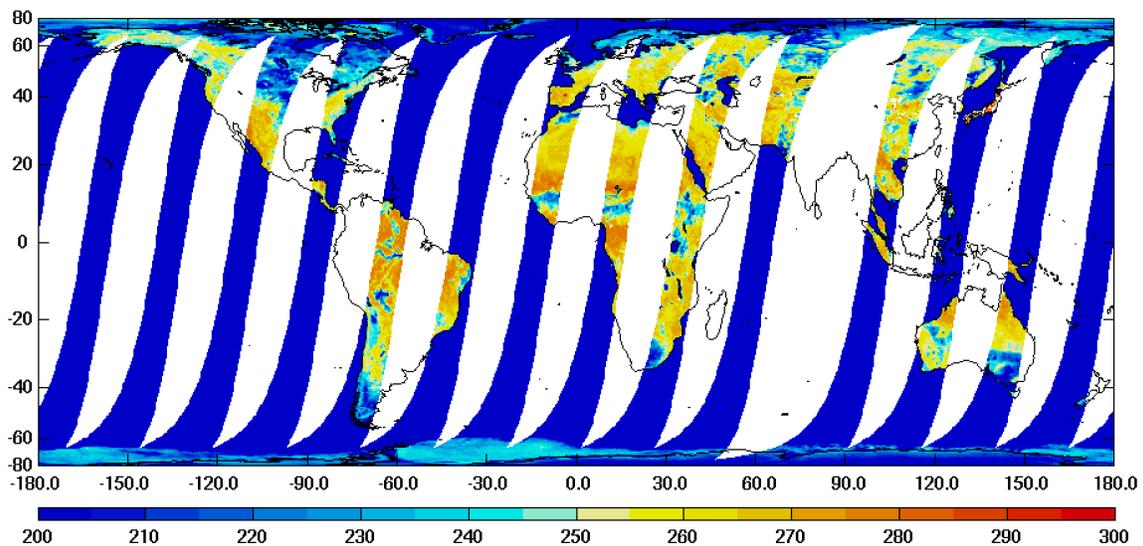
Figure 12.4: Descending aft-look H-polarized TB on Global Cylindrical EASE-Grid 2.0 projection.
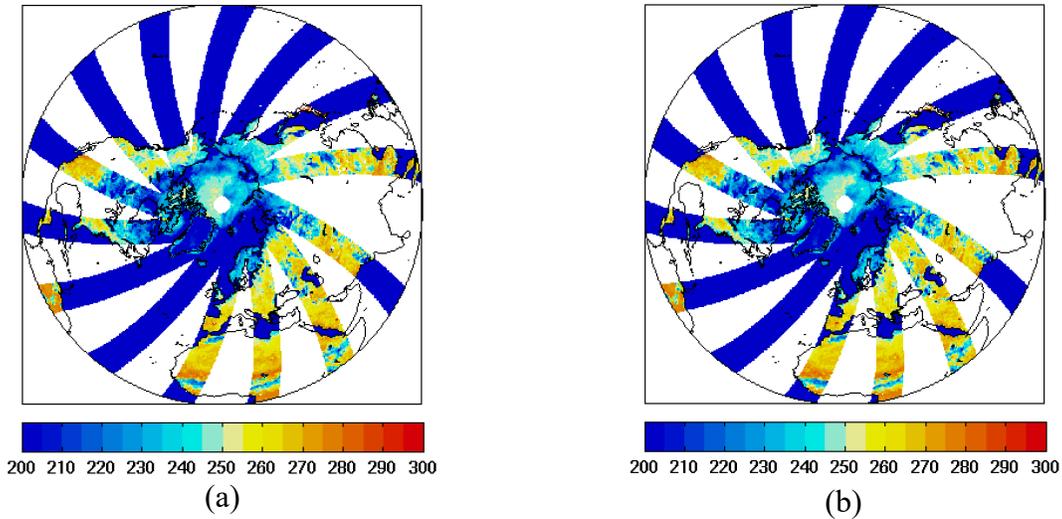
41

Figure 12.5: (a) Descending fore-look H-polarized TB on North Polar EASE-Grid 2.0 projection. (b) Descending aft-look H-polarized TB on North Polar EASE-Grid 2.0 projection.
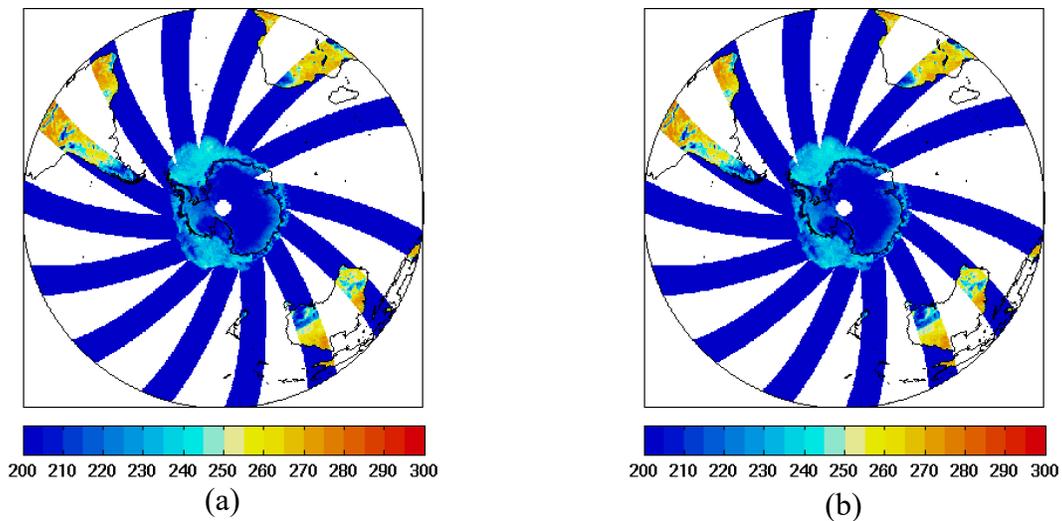
Figure 12.6: (a) Descending fore-look H-polarized TB on South Polar EASE-Grid 2.0 projection. (b) Descending aft-look H-polarized TB on South Polar EASE-Grid 2.0 projection.

The L1C_TB gridded product now screens all L1B_TB brightness temperature data using bit 0 of the quality flag. Only footprints with bit 0 of the quality flag set to 0 and TB value not equal to FillValue are used in the binning and averaging/interpolation process.

12.2 Enhanced L1C_TB_E Product

The enhanced L1C_TB_E product is an optimally interpolated product from the L1B_TB swath product onto a 9-km EASE Grid 2.0 fixed Earth grid. The interpolation is optimal in the sense that the data are closest to what would have been measured had the instrument actually made its

measurements at the interpolation points. The algorithm theory is described in the ATBD [12.2]. The data were analyzed for NEDT, calibration bias, and spatial and spectral characteristics.

12.2.1 NEDT

NEDT was assess over the ocean using several methods. Data are from orbit 5962 descending. Results for the brightness temperature field shown in Fig. 12.1(a) are shown in Table 12.1.

Table 12.1. NEDT estimates for the three Level 1 products:

Methodology	NEDT (K)	Product
Standard deviation of samples within bounding box	1.14 0.77 0.77	L1B_TB L1C_TB L1C_TB_E
Mean of Allen deviation of antenna scans across bounding box	1.06	L1B_TB
Mean of standard deviation of columns within bounding box	0.71 0.73	L1C_TB L1C_TB_E
Mean of Allen deviation of columns within bounding box	0.72 0.67	L1C_TB L1C_TB_E

The L1C_TB_E product has NEDT similar to L1C_TB. The L1C products have 60% the standard deviation of the L1B product because of the effects of averaging and/or interpolating. Because L1C_TB_E is oversampled, NEDT noise in adjacent samples is partially correlated. Using the same data, the correlation function was estimated for this dataset and is shown in Fig. 12.1(b).
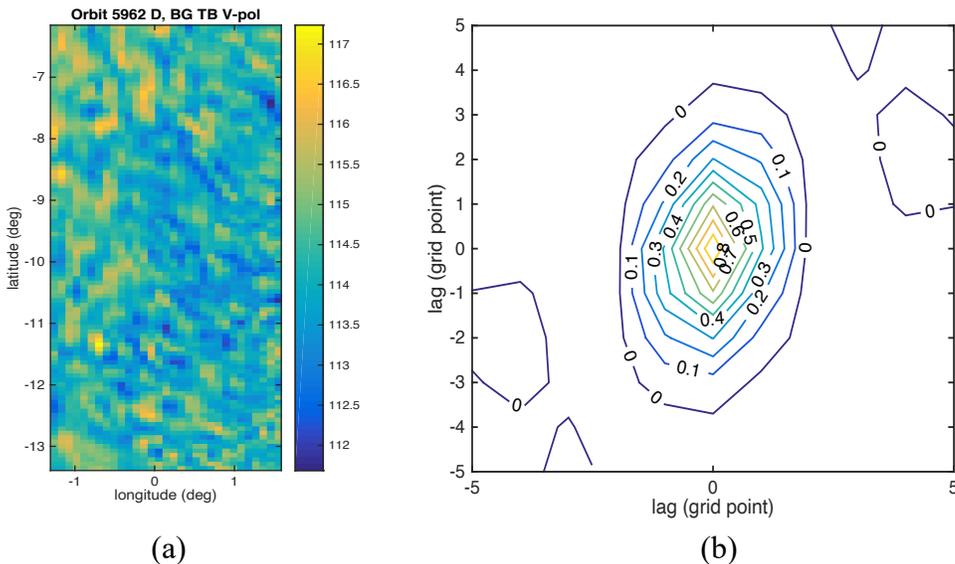

(a) (b)

Figure 12.1. (a) Ocean brightness temperature field selected from L1C_TB_E half-orbit 5962D. (b) Noise correlation estimate of field shown in (a).

12.2.2 Calibration Bias

The L1C_TB_E surface brightness temperature (TB) and top-of-ionosphere (TOI) apparent temperature outputs are compared with L1B_TB to verify consistent calibration of Level 1 processes. There is a small difference of +/- 0.003 K in TB calibration over the ocean between L1B_TB and L1C_TB_E shown in Figure 12.2(a). The TOI temperature is also used to demonstrate the consistency between the two products. As evident in Fig. 12.2(b), the relative biases between L1C_TB_E and L1B_TB track fairly consistently with each other, showing little dependence on polarization or azimuth. The sources of the small differences in TB and the seasonal change in TOI are being investigated. One candidate is the difference in ancillary data (e.g., sea surface temperature, surface pressure and humidity) used during the processing software execution. Some of the ancillary data products are forecasts and others are reanalysis.
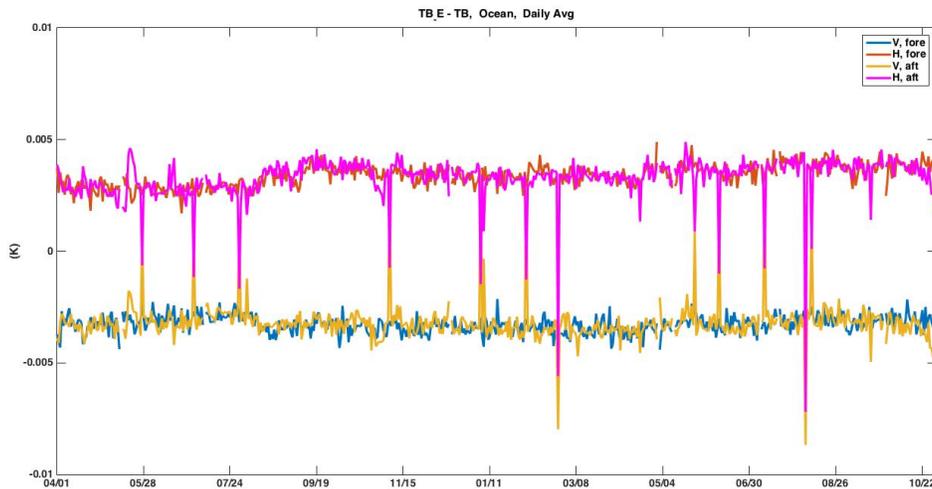
(a)
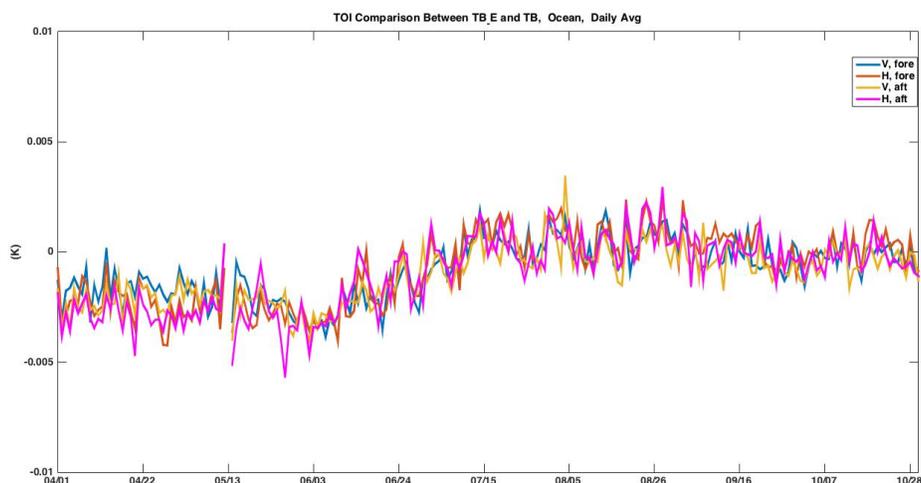
(b)

Figure 12.2. Daily globally-averaged difference over ocean between L1B_TB and L1C_TB_E. (a) TB difference at ocean surface. The difference is +/- 0.003 K. The difference relative to ~100 K ocean TB is +/- 30 ppm. (b) Apparent temperature difference at the on top of ionosphere.

12.2.3 Spatial Analysis

There are across-swath artifacts <0.1 K and larger coastline differences between L1B_TB and L1C_TB_E shown in Fig.12.3. The differences may be due to certain particular configuration parameters (e.g. the number of points and their locations used in BG interpolation) currently implemented in L1C_TB_E processing or and discrepancy in ancillary data used by the two products at the time of this analysis. The differences are being investigated.
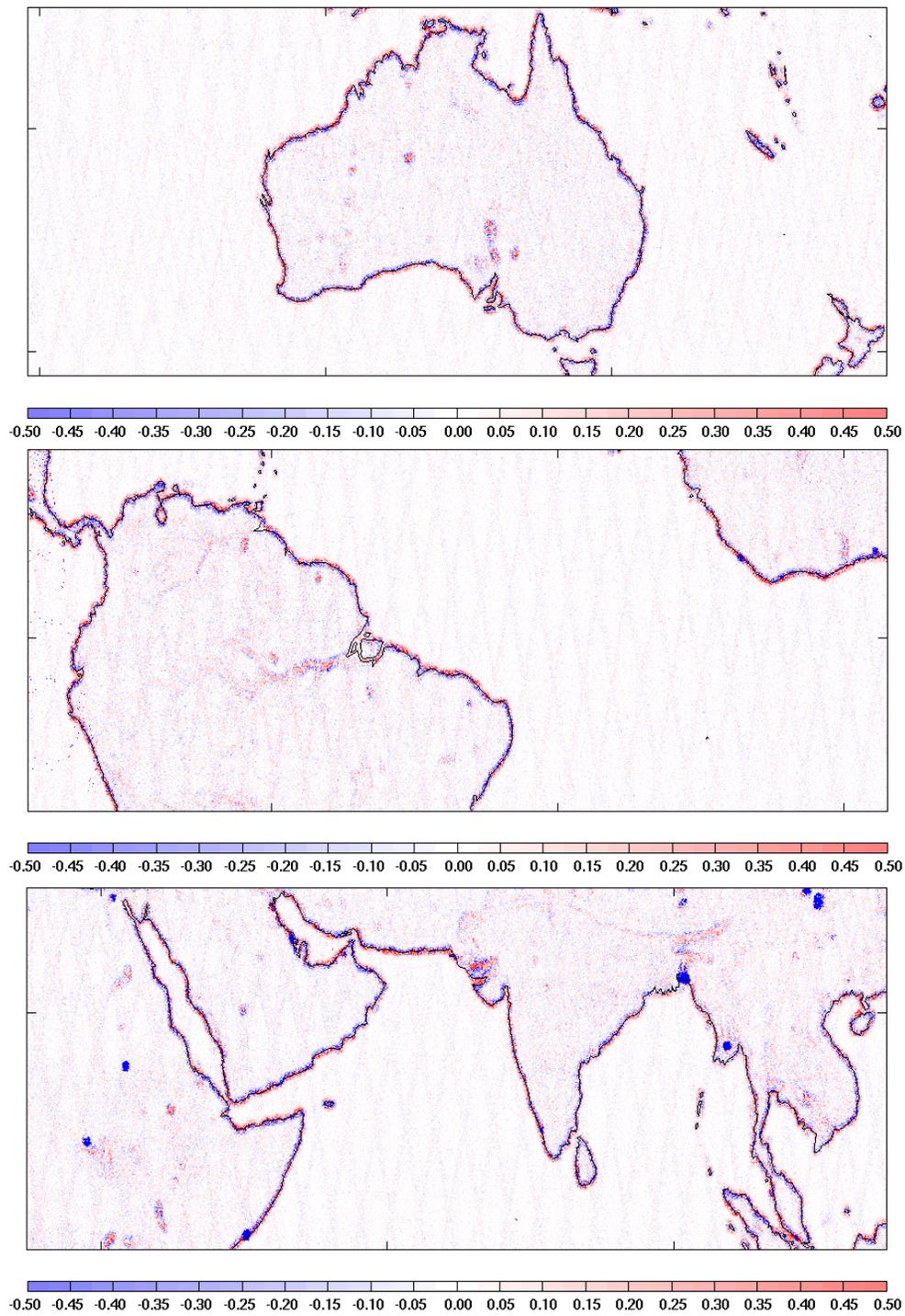
Figure 12.3. Differences between L1C_TB_E and L1B_TB after space-time matchup running April 1, 2015 and Oct 30, 2016, showing across-swath and coastline artifacts.

12.2.4 Spectral Analysis

The 9-km sampling and interpolation in the L1C_TB_E data ensures the spatial spectrum is not aliased in the gridding process. The standard L1C_TB product, however, does not have this feature. The impacts in the spectral domain can be seen in Figure 12.4 (c). The 36-km sampled product shown in Fig. 12.4(b) has high-frequency content aliased into the low frequencies, whereas the new enhanced product (L1C_TB_E) preserves the high-frequency content.
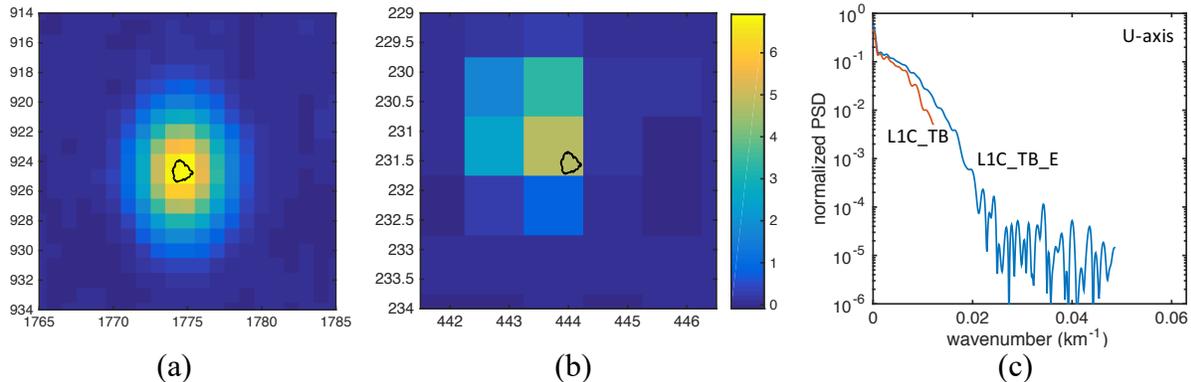

(a)	(b)	(c)

Figure 12.4. Annually-averaged brightness temperature (background-removed) of Ascension Island sampled at (a) 9-km and (b) 36-km. Color scale is in Kelvins and coordinates are EASE-grid indices. The spatial frequency response of the horizontal axis is shown (c). Note the maximum wavenumber for each spectrum is limited by the sampling period and the spectrum of the 36-km sampled data underestimates the power-spectrum at wavenumbers > 0.01 km^{-1}.

References

[12.1] Brodzik, M. J., B. Billingsley, T. Haran, B. Raup, M. H. Savoie. "EASE-Grid 2.0: Incremental but Significant Improvements for Earth-Gridded Data Sets," *ISPRS International Journal of Geo- Information*. 2012; 1(1): 32-45.

[12.2] SMAP Project, JPL D-72545, NASA Jet Propulsion Laboratory, Pasadena, CA., July 14, 2015

[12.2] Chaubell, et al., Algorithm Theoretical Basis Document (ATBD) SMAP Enhanced L1C Radiometer Half-Orbit 9 km EASE-Grid Brightness Temperatures, 2016. [Online.] https://nsidc.org/data/SPL1CTB_E/.

13 Verification

The validated data meet the SMAP error budget requirement. The error budget for an L1B_TB footprint is 1.8 K rms over land. The equivalent error budget is 1.4 K over ocean (due to reduced NEDT). The error budget includes NEDT, errors in radiometric calibration, calibration drift and errors in geophysical corrections. The error budget is verified on orbit by measuring NEDT and comparing to the ocean model.

NEDT: The allocation to NEDT is 1.6 and 1.1 K rms over land and ocean, respectively. The measured NEDT is 1.1 K rms over land and 0.9 K over ocean (in TB).

The calibration is allowed to drift up to 0.4 K / month with respect to the ocean model. These data show changes of < 0.10 K (after correction) for the entire available data set.

14 Outlook and Future Plans

The SMAP radiometer Version 5 calibration performance shows significant improvements. We will track the radome emissivity and assess the varying calibration impact of the radome paint degradation over the years. In addition we will analyze and correct observed geolocation error, potentially caused by the antenna pattern and spacecraft attitude.

15 Acknowledgments

This document resulted from the many hours of diligent analyses and constructive discussion among members of the SMAP radiometer hardware team, algorithm development team and science team.